Catalysis Science & Technology

ROYAL SOCIETY OF CHEMISTRY

REVIEW

View Article Online
View Journal | View Issue

Cite this: *Catal. Sci. Technol.*, 2024, **14**, 5525

Recent advances in selective methanol oxidation electrocatalysts for the co-production of hydrogen and value-added formate†

Jiaxin Li, Hongmei Yu, * Jingchen Na, Senyuan Jia, Yutong Zhao, Kaiqiu Lv, Wenzhuo Zhang, Jun Chi and Zhigang Shao *

Traditional water splitting is significantly impeded by the sluggish kinetics and large overpotential of the anodic oxygen evolution reaction (OER). Accordingly, replacing the OER with a more thermodynamically favorable organic substance oxidation reaction to combine with the hydrogen evolution reaction (HER) is an innovative strategy to obtain green hydrogen. In this case, the electro-reforming of methanol coupled with the electrochemical HER can realize the energy-saving co-generation of value-added formate and hydrogen. Therefore, controlling the process of methanol oxidation and making it selectively transform to formate have become a worthy topic. Thus far, various catalysts and modification strategies have been developed for the selective methanol oxidation reaction (SMOR). Transition metal-based materials are the most studied catalysts because their moderate catalytic ability can better control the process of methanol oxidation. Electronic structure modulation is the most efficient strategy to improve the SMOR performance of catalysts. However, few systematic reviews on the SMOR have been reported. In light of significant advances achieved recently, herein, we reviewed the recent advances in SMOR electrocatalysts for the co-production of value-added formate and green hydrogen. In particular, the mechanism of the SMOR is initially introduced, including the traditional surface adsorption mechanism and the newly developed lattice oxygen participation mechanism. Subsequently, strategies for catalyst design are analyzed from the aspects of chemical bond activation/inhibition, electronic structure manipulation, dual active site construction, and increasing the number of active sites. Thereafter, performance descriptors involving electrochemical measurements and product detection are discussed to show the basic evaluation criterion, and various catalysts for the SMOR are categorized according to their composition to display the development of catalysts. Finally, conclusions and perspectives are presented. We hope that this comprehensive effort will be helpful in the literature survey of the SMOR and provide inspiration to the SMOR research community, attracting more attention to the electro-upgradation of organic substances coupled with green hydrogen generation.

Received 8th June 2024,
Accepted 9th August 2024

DOI: 10.1039/d4cy00727a

rsc.li/catalysis

1. Introduction

Generating "green hydrogen" from water electrolysis powered by renewable energy is considered an ideal hydrogen production method that is devoid of energy depletion and environmental pollution.[1–3] However, the sluggish kinetics and large overpotential of the anodic oxygen evolution reaction (OER) largely impede the cost-efficiency of overall water splitting (OWS).[4,5] Although the theoretical equilibrium potential of OWS is 1.23 V, the applied voltage in practical use may increase to as high as 1.8–2.0 V to overcome the thermodynamic barrier and extra resistance.[6,7] It has been reported that 94.5% of the total energy input for OWS is consumed by the OER.[8] Consequently, various catalysts have been explored to achieve higher reaction efficiency.[9,10] However, another concern is that the anodic product of O_2 is less valuable and will inevitably mix with H_2 in the cathode, leading to the risk of explosion.[11] Thus, to alleviate these limitations, several oxidation reactions of organic substrates have been explored for substituting the OER, such as alcohols, aldehydes, and urea.[12–16] These biomass oxidations are more thermodynamically favorable and can lower overpotential while presenting additional benefits such as high value-added products and pollutant degradation, which

Fuel Cell System and Engineering Laboratory, Dalian Institute of Chemical Physics, Chinese Academy of Sciences, Dalian 116023, Liaoning, China.
E-mail: hmyu@dicp.ac.cn, zhgshao@dicp.ac.cn

† Electronic supplementary information (ESI) available. See DOI: https://doi.org/10.1039/d4cy00727a

have become research hotspots in recent years.[17–20] Guo's group reported a comprehensive review on chemical-assisted water splitting with the concurrent evolution of H_2 and high value-added chemicals.[21] Their review introduced different alternative chemicals at the anode, especially for small molecules that can be produced from biomass.

Among the alternative organic substrates, methanol is the most important liquid C1 resource, which has attracted significant attention due to its simple structure, large aqueous solubility, high volumetric energy density (15.9 MJ L^{-1}), good oxidation reactivity, and extensive resources.[22–24] The methanol oxidation reaction (MOR) has long been used in direct methanol fuel cells (DMFCs)[25–28] and methanol-assisted water splitting.[29–31] However, the focus is mainly on enhancing the power output and catalytic performance by completely oxidizing methanol, whose product is the environmentally unfriendly CO_2. In recent years, increasing attention has been paid to partially oxidizing methanol to formate, which has a higher economic value of *ca.* 1300 $ per ton than that of methanol (350 € per ton).[32] The standard potential for the electro-oxidation of methanol to formate is reported to be as low as 0.103 V *vs.* SHE, which is much lower than that of OER.[32] Besides, the MOR proceeding *via* the formate pathway still yields an energy density of 9.2 MJ L^{-1}, which is slightly higher than that of liquid hydrogen (8 MJ L^{-1}).[33] Moreover, the methanol-to-formate route offers several economic and practical benefits, particularly in the fields of chemical production and environmental sustainability. Formate is one of the basic organic chemical raw materials and has been widely used in the pharmaceutical, leather, rubber, textile, and pesticide industries.[34,35] The conversion of methanol to formate also can be integrated into carbon capture and utilization (CCU) strategies. Methanol can be synthesized from captured CO_2, which is then transformed into formate, thus providing a sustainable loop for carbon utilization. Therefore, it is a promising way to replace OER with the selective methanol oxidation reaction (SMOR) to formate for anodic chemical upgrading and cathodic hydrogen production. Moreover, SMOR provides a green sustainable method for chemical synthesis superior to industrial manufacturing with complex procedures and high energy consumption.[36–39]

In 2003, the formate pathway in the methanol electro-oxidation process was discovered.[40] *In situ* surface-enhanced IR absorption spectroscopy revealed the symmetric stretching of formate species on the surface of Pt. However, the systematic study on SMOR to formate is less than ten years. It was only in 2020 that the number of relevant reports started to rapidly increase, with various catalysts and modification methods reported. Pt-, Ru-, and Pd-based materials are the most active catalysts for MOR,[41,42] but their resource scarcity, high cost, and CO poisoning issues severely restrict their widespread application.[43] Moreover, these noble metals tend to completely oxidize methanol to CO_2. Alternatively, non-noble metal-based catalysts have been widely studied for SMOR. Because of their mild catalytic activity, the process of SMOR can be easily modulated. Among the non-noble metals, Ni is the most frequently used, followed by Co, Fe, Cu, and Mo. For example, an NiCo layered double hydroxide (LDH) was reported to have a high faradaic efficiency for methanol to formate ($FE_{formate}$) of over 95% at a wide potential range.[44] The Ni^{3+} species formed during the electrochemical oxidation were believed to be the active sites. Moreover, the ultrathin morphology was beneficial for the creation of oxygen vacancy, which could lower the energy barrier for methanol oxidation. In another study on Fe-incorporated NiCo-LDH for SMOR,[45] Co was proven to reduce the potential required for the Ni^{2+}/Ni^{3+} redox *via* the coordinating effect. Most importantly, Fe was found to act as an "electron pump", where it underwent valence changes and accelerated the electron transfer. As a result, a current density of 10 mA cm^{-2} was achieved at only 1.349 V *vs.* RHE and the $FE_{formate}$ reached about 95%.

Considering the great potential of methanol upgrading to value-added chemicals coupled with green hydrogen generation in energy and environmentally relevant application, many technology advances have been made including catalyst synthesis, design strategy, catalytic mechanism, and practical application. Recently, Zhu's group reviewed the study of simultaneous production of hydrogen and formate by coupling the hydrogen evolution reaction (HER) and methanol oxidation reaction (MOR).[46] They summarized the concept, fundamental electrochemistry of MOR, materials design and development of the methanol–water hybrid electrolysis. However, they only analyzed Ni-based electrocatalysts in alkaline medium. Herein, we mainly focus on the selectivity and process control of SMOR. In addition, all types of catalysts reported in recent years and the prevailing evaluation descriptors are included to make our work more comprehensive. Firstly, we present the mechanism and catalyst design strategies of SMOR with a focus on the reaction process control of methanol oxidation and the selective production of formate. Then, the catalytic performance descriptors and catalyst development are summarized to give an overview of the advancement in research. Finally, the problems, challenges, and perspectives are provided on this significant topic. We believe this review can be instructive for SMOR research and provide reference to the community devoted to the co-production of value-added chemicals and green hydrogen.

2. Mechanism of selective methanol oxidation reaction

To better control the SMOR and achieve higher selectivity, it is necessary to understand the reaction process of MOR and identify the intermediates. In fact, many pioneering research articles and critical reviews have conducted sufficient studies on the mechanism of methanol oxidation.[47–50] Thus, we will not repeat it in detail and just give a brief description. The complete oxidation of methanol at the anode can be described by the following equation: $CH_3OH + 6OH^- \rightarrow CO_2$

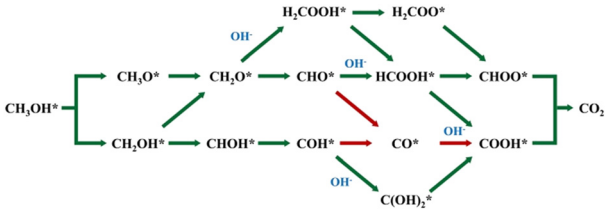

Fig. 1 Possible reaction pathways and intermediates of the MOR, where * represents the active site of the catalyst.

+ $5H_2O$ + $6e^-$.[51] The specific reaction mechanism can be broadly classified into two routes, namely the indirect way with CO* as a poisoning intermediate and the direct way without CO* formation (Fig. 1). It can be seen that the diversion of these two ways originates from the different dehydrogenation sites on methanol molecules. Thus, facilitating the fracture of the O–H bond of methanol to undergo the direct way at the initial stage and suppress the further transformation to CO_2 at the final stage will be helpful for the generation of formate and improve its selectivity.[52] SMOR is actually the partial oxidation of methanol. The electrooxidation of methanol to formate is a four-electron transfer process, as follows: $CH_3OH + 5OH^- \rightarrow HCOO^- + 4H_2O + 4e^-$.

It is known that noble metals such as Pt and Pd generally facilitate the complete oxidation of methanol to form CO_2; conversely, transition metals are more suitable to electrocatalyze methanol to formate due to their moderate activity. Therefore, the catalytic mechanism of SMOR on transition metals is mainly introduced here. The *in situ*-formed high valent transition metal species are believed to be the active phases in many anodic organic upgrading reactions,[53–55] which is also applicable for SMOR. In a study on SMOR catalyzed by CoO–$Ni(OH)_2$ nanosheets grown on MOF-derived carbon nanotube arrays (CNTs@CoO–$Ni(OH)_2$),[56] *in situ* Raman spectroscopy detected two peaks located at 475 and 560 cm^{-1}, corresponding to the Ni–O bending and Ni–O stretching vibration of Ni^{3+}OOH in the background KOH solution, respectively (Fig. 2a). However, Ni^{3+}OOH peaks were not found in the SMOR process, indicating its fast consumption in the presence of methanol. Thus, an indirect mechanism of SMOR involving the interaction between Ni^{3+}-OOH and methanol was assumed, where Ni^{3+}OOH species was first electrochemically generated from the pre-catalyst, and then chemically oxidized the methanol molecules (Fig. 2b). A similar conclusion that Ni^{3+}OOH is the active site for the oxidation of alcohols can also be seen in other reports.[57,58] Zhu *et al.* further proposed the combined active sites in Ni^{3+}OOH, where Ni^{3+} and the nearby electrophilic oxygen species cooperatively promoted SMOR.[32] In particular, the exposed Ni^{3+} species provided adsorption sites for methanol, while the nearby electrophilic oxygen acted as a hydrogen acceptor, resulting in concerted hydrogen-transfer from methanol to the catalyst. Fu's group claimed the significant synergistic effect of foreign species with NiOOH.[59] They synthesized hollow NiSe supported on carbon nanotubes (h-NiSe/CNTs) for the co-production of H_2 and formate *via* electrocatalytic methanol upgrading. The *in situ*-formed NiOOH still acted as the active site to break the O–H bond to form the Ni–OCH_3 intermediate. Meanwhile, SeO_x and NiOOH were revealed to collaboratively tune the d-band center of the catalyst to optimize the adsorption energy during the SMOR process and inhibit the further oxidation of formate to CO_2, thereby achieving high selectivity. In addition to SeO_x, the incorporation of Co and FeCo in NiOOH was also proven to be efficient to SMOR with $Ni_{0.9}Co_{0.1}Se$ and FeCoNi disulfide as pre-catalysts, respectively.[60,61] In fact, the phase transformation on the catalyst surface during the electrocatalytic process is well recognized as surface reconstruction. Especially in the case of transition metals with multiple valences, high valent species are usually formed during the surface reconstruction and act as the real active phases. The surface reconstruction is indeed significant to improve the catalytic activity of pre-catalysts, and different pre-catalysts have different abilities for surface reconstruction, thus varying catalytic performances were observed.[62] Therefore, the pre-catalysts should be designed to be more inclined to undergo surface reconstruction. Strategies should be performed to accelerate the redox reactions between low and high valent species, reduce the energy barrier for the formation of active phases, and then promote surface reconstruction.

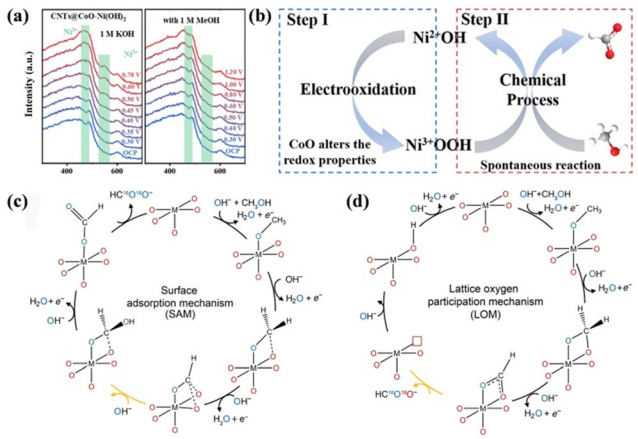

Fig. 2 (a) *In situ* Raman spectra of the OER and MOR for CNTs@CoO–$Ni(OH)_2$. (b) Dynamic reconstruction of the active Ni^{3+}OOH layer.[56] Reproduced from ref. 56 with permission from the Royal Society of Chemistry, Copyright 2023. Possible reaction mechanisms for (c) SAM and (d) LOM.[63] Reproduced from ref. 63 with permission from American Association for the Advancement of Science, Copyright 2023.

The above-mentioned mechanism was explained by the adsorption/desorption relationship between reactants and active sites. Recently, Meng *et al.* proposed a novel mechanism involving the participation of lattice oxygen.[63] The authors fabricated ^{18}O isotope-labeled $SrCoO_{3-\sigma}$ and NiO_xH_y catalysts to explore the origin of the O atoms in formate. Gas chromatography-mass spectrometry (GCMS)

measurement detected the presence of $HC^{16}O^{18}OH$ with one oxygen atom from the oxide lattice, which required the formation of oxygen vacancies and the activation of lattice oxygen during SMOR. Thus, the lattice oxygen participation mechanism (LOM) was proven, which is different from the surface adsorption mechanism (SAM). In the SAM mechanism, deprotonation occurred in the first three steps to form the *CHO intermediate, and then successive attack of hydroxide happened in the following two steps to generate $HC^{16}O^{16}O^{-}$ (Fig. 2c). In the LOM mechanism, the first three steps were the same as that in SAM, but then the attacking species shifted from OH^{-} to lattice oxygen, accompanied with the formation of $*^{16}O^{18}OCH$ and the creation of oxygen vacancies (Fig. 2d). Moreover, the lower rate-determining step (RDS) energy barrier for the LOM was confirmed by density functional theory (DFT) calculation, which was superior to the SAM.

3. Strategies for catalyst design

3.1 Chemical bond activation and inhibition

As mentioned in the part on the mechanism, whether the C–H bond or the O–H bond breaks at the beginning of the reaction results in the complicated catalytic kinetics and process of SMOR. It is beneficial for realizing highly efficient SMOR to formate by proceeding through the non-CO pathway by facilitating the cleavage of the O–H bond on the methanol molecule. Thus, exploring catalysts that tend to break the O–H bond is significant for improving the SMOR performance. In the research by Zhou *et al.*, a partial pyrolyzation treatment was conducted to modify Ni-MOFs for methanol chemical upgradation, presenting insight into the variation in the reaction energy.[64] Different from the fully carbonized products, the partially pyrolyzed Ni-MOFs obtained at 350 °C (Ni-MOFs@350) not only well inherited the porous properties, but also exhibited good conductivity. Most importantly, the Ni–O coordination number decreased from 6 (Ni-MOFs) to 3.92 (Ni-MOFs@350). By computing the Gibbs free energy for each fundamental step in the direct way (O–H activation, OHA) and the indirect way (C–H activation, CHA) (Fig. 3a–c), the energy steps in the OHA route were found to have a mild fluctuation in relation to CHA, indicating its more favorable thermodynamics under the catalysis of Ni-MOFs@350. As a result, only 1.37 V *vs.* RHE was required to achieve 100 mA cm^{-2} for SMOR, and the $FE_{formate}$ reached up to 98.4% benefiting from the modulation of O–H activation.

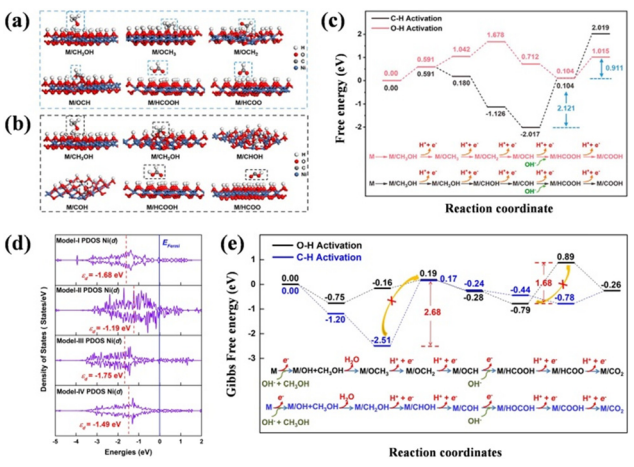

Fig. 3 Intermediate adsorption configurations on NiOOH in (a) OHA and (b) CHA pathways. (c) Free energy diagram through the OHA and CHA routes.[64] Reproduced from ref. 64 with permission from the American Chemical Society, Copyright 2023. (d) Corresponding projected density of states (PDOS) of model-I-SO_x/NiOOH, model-II-Ni, model-III-SO_x, and model-IV-SO_x/Ni. (e) Gibbs free energy diagrams for methanol conversion on the modeled Ni_3S_2 surface.[65] Reproduced from ref. 65 with permission from Elsevier, Copyright 2021.

In addition to promoting the generation of formate, preventing its further transformation is also important to control the methanol oxidation process. Generally, it is challenging to balance high activity and high selectivity because highly efficient catalysts prefer to fully oxidize methanol to CO_2 rather than an intermediate. Thus, suppressing the overoxidation of formate to CO_2 is significant for SMOR. To achieve the two targets in one stroke, Fu's group constructed a defect-rich Ni_3S_2-CNF catalyst to improve methanol-to-formate without CO_2 production at large current densities.[65] The $FE_{formate}$ was kept beyond 90% in the wide potential range of 1.32–2.02 V with the current density above 700 mA cm^{-2}. The synergism of the *in situ* formed NiOOH and SO_x tuned the d-band center of Ni_3S_2, which inhibited the further oxidation to CO_2 and gained high selectivity. As shown by the projected density of states (PDOS) (Fig. 3d), the Ni d-band center of SO_x/NiOOH (−1.68 eV) was between that of Ni (−1.19 eV) and SO_x (−1.75 eV). According to the Sabatier principle,[66,67] the active sites with neither too strong nor too weak adsorption of intermediates are more favorable, and this adsorption behavior can be affected by adjusting the d-band center.[68] Thus, SO_x/NiOOH with a moderate adsorption energy well maintained the balance of reducing the energy barrier and facilitating the intermediate product release. Regarding the step of electron loss from M/HCOOH to M/HCOO, an uphill energy barrier of 1.68 eV was needed, as proven by DFT calculation (Fig. 3e), which made it difficult to further transfer to the final product of CO_2, leading to high SMOR activity and selectivity. In another study by Fu's group, the unique NiSe (102) facets were selectively exposed in the presence of carbon nanofibers (CNFs@NiSe) through one-pot hot injection.[69] The increased exposure of NiSe (102) was confirmed to prevent the further oxidation of formate by requiring a large energy barrier (1.21 eV). Thus, a high $FE_{formate}$ of 97.9% was achieved.

It can be seen that the activation and inhibition of chemical bonds during methanol oxidation were mainly realized by regulating the coordination number, d-band center, and crystal facet orientation. However, the interaction between them is ambiguous, and thus a more specific and quantitative descriptor such as the "volcano plot" of OER

should be proposed to better guide the design and prediction of catalysts for SMOR.

3.2 Electronic structure manipulation

Acting as a surface-sensitive reaction, SMOR has a close relationship with the electron distribution and chemical environment of the catalyst. It has been reported that the tuning of the electron structure of the catalyst can improve its electrical conductivity, optimize the binding energy of intermediates, and even reconstruct the active centre.[70–72] According to the d-band centre theory, the position of the d-band centre is relative to the Fermi level, which plays a crucial role in determining the adsorption properties of the catalyst.[73] By tuning the d-band centre, the binding energies of the intermediates can be optimized for enhanced catalytic activity. The electron redistribution and electron density shift can be modulated by integrating elements with different electronic properties or by modifying the catalyst structure.[74] Moreover, geometric effects that involve the arrangement and coordination of atoms on the catalyst surface can also tune the electron configuration.[75] In the case of SMOR, electronic structure manipulation is a frequently used strategy to generate an appropriate adsorption energy, reduce the energy barrier, and improve the catalytic performance. Techniques such as hetero-atom doping, vacancy/defect creation, and heterostructure construction are all effective strategies to manipulate the electronic structure.

3.2.1 Hetero-atom doping. Heteroatom doping has been universally acknowledged as an efficient catalyst modification method by introducing foreign atoms into the lattice of the host catalyst.[76,77] The replacement of the parental atoms with dopants can introduce favorable physicochemical characteristics such as tuning the electron distribution, altering the morphology, and improving the conductivity.[78,79] Both metal and non-metal atoms have been employed as dopants for SMOR. For example, Ni-doped MoN deposited on Ni foam (Ni-MoN/NF) was synthesized *via* a two-step hydrothermal annealing process for integrated SMOR and HER.[80] The electronic structure of MoN was tuned by Ni doping, as proven by DFT calculation, which lowered the reactant molecule adsorption energy and accelerated the elementary reaction steps. As a result, only 1.48 V *vs.* RHE was required to deliver the current density of 100 mA cm^{-2} for SMOR and an $FE_{formate}$ of up to 95% at the anode and $FE_{hydrogen}$ of 100% at the cathode were achieved. In the case of non-metal atom doping, a flower-like S-doped NiCo-LDH was prepared by combined ultrasonic and sulfurization treatment for SMOR.[81] The sulfur with a low coordination number acted as the promoter for methanol oxidation by modulating the electronic configuration and improving the conductivity. The potential at 100 mA cm^{-2} decreased to 1.39 V *vs.* RHE and an $FE_{formate}$ of nearly 100% was maintained at a high current density of 300 mA cm^{-2}. Thus far, all the doped catalysts used for SMOR are single-element doped and the dopants are limited. Alternatively, the co-doping of two elements may better display the synergistic effect, and more elements are expected to be involved to induce more attractive properties of the catalyst. In addition, the role of doping needs to be further studied, such as the effect of dopants on the lattice distortion and coordination environment.

3.2.2 Vacancy/defect creation. The electronic configuration of the catalyst can be tuned by compositional variation and structure adjusting. Creating defects is one of the most efficient strategies for generating distortion in a perfect crystal structure. Compared to the ideal crystal lattice, the defective sites usually exhibit unique atom arrangements and electronic structures,[82–84] which can induce new properties and even act as anchor points to capture reactive species to form new active centers,[85] and especially beneficial for the SMOR process with multiple intermediate products. It was reported that the oxygen vacancy, hydroxyl vacancy, and cationic vacancy all had a promoted function for SMOR.[86–88] Oxygen-vacancy-rich CuO supported on copper foam (V_O-rich CuO/CF) was prepared by ultrasonication-assisted acid etching for alcohol upgrading.[86] The *in situ*-formed V_O was revealed to alter the electron distribution and chemical environment of the catalyst surface, thereby optimizing the

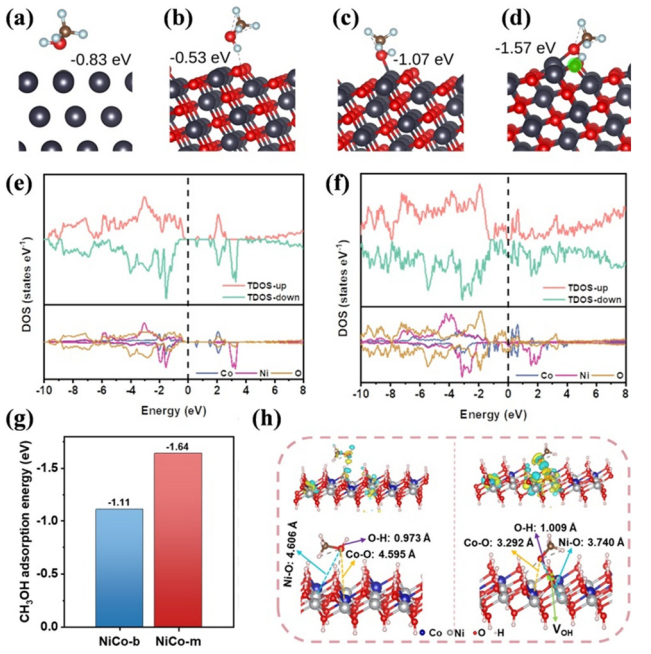

Fig. 4 (a) Cu(111), (b) pristine CuO (111) for interaction with the H atom, (c) pristine CuO (111) for interaction with the O atom, and (d) O-vacant CuO (111) for interaction with the O atom. The position of the V_O is highlighted in green. The binding energy is given in each case.[86] Reproduced from ref. 86 with permission from Springer Nature, Copyright 2022. Total and partial density of states (TDOS and PDOS) for (e) NiCo-b and (f) NiCo-m. (g) DFT-calculated adsorption energies of CH_3OH on the surfaces of the NiCo-LDHs with and without V_{OH} and (h) models of CH_3OH adsorbed on the surfaces of the NiCo-LDHs with and without V_{OH}, and the differential charge density images of NiCo-LDHs with and without V_{OH} adsorbing CH_3OH.[87] Reproduced from ref. 87 with permission from Elsevier, Copyright 2022.

adsorption behavior of methanol. As calculated, the bonding between the O-vacant CuO (111) and methanol molecule was strong and energetically favorable (Fig. 4a–d). Therefore, a high turnover frequency was obtained accompanied by a stable operation of 24 h at the current density beyond 200 mA cm^{-2}. Meanwhile, the optimized $FE_{formate}$ of ~99% was achieved at 1.82 V *vs.* RHE. Hydroxyl vacancy (V_{OH}) was reported to enhance the density of states (DOS) near the Fermi level of monolayered NiCo-LDHs (NiCo-m) compared to the counterpart of bulk NiCo-LDHs (NiCo-b), and then improve the electrical conductivity to yield fast charge transfer (Fig. 4e and f).[87] Furthermore, the adsorption energy of methanol on NiCo-m with V_{OH} was calculated to be 1.64 eV, which is larger than that of NiCo-b (1.11 eV), indicating the more favorable adsorption of methanol (Fig. 4g). Moreover, the distance between O and Ni/Co for NiCo-m was shortened, while the O–H bond was lengthened (Fig. 4h), revealing the enhanced interaction between the adsorbed CH_3OH and NiCo-m as well as the easier dehydrogenation of CH_3OH. Due to these properties, an improved SMOR catalytic performance was obtained with a low overpotential and high kinetics. Similarly, a cationic vacancy was introduced by doping B into $CuCo_2O_4$ (B/$CuCo_2O_4$), and the as-prepared catalyst delivered a high current density by improving the methanol absorption ability.[88] In addition, carbon defect was reported to be beneficial for methanol oxidation. In the study of carbon nanotube (CNT)-supported Pt nanoparticle catalysts,[89] the functional CNT defects caused the spontaneous deposition of Pt, better anchoring the active species. The CNT defects also displayed high reactivity because they were easier to be oxidized to oxygen-containing species, which improved the anti-poisoning ability. As is known, there are various types of defects, including point defects, line defects, planar defects, and volume defects,[90] and the defect size and concentration also play notable roles in catalytic performance.[91] Moreover, the surface defect, subsurface defects and bulk defects based on the location of defects also have a big influence on catalytic activity. For example, Wei *et al.* innovatively constructed subsurface V_O in a metallic In-embedded In_2O_3 nanoflake catalyst for the CO_2 reduction reaction.[92] Unlike the surface defects and bulk defects, the oxygen defects in this work were located at the interface between In and In_2O_3. The resultant O–In–(O)Vo-In–In structure featuring large-size defect complexes induced the electron-delocalization effect, by which the electrons were extracted from subsurface oxygen defects to the surface active sites. This electron transfer promoted the electronic coupling with the reactant and stabilized the intermediate, which was beneficial for improving the selectivity. Thus, more types of defects with distinct properties for SMOR are worthy of in-depth research.

3.2.3 Heterostructure construction. Among the various alternative oxidants at the anode of water electrolysis including alcohols, aldehydes, and urea, the reaction site is the nucleophilic groups of hydroxyl, aldehyde, and amino in the corresponding organic substrates.[93,94] Thus, creating an electrophilic domain on the catalyst may be helpful to promote the adsorption and decomposition of the nucleophilic groups of the reactants, thereby boosting the activity. Fortunately, constructing heterostructure catalysts with a hetero-interface can form a built-in electric field containing electrophilic and nucleophilic regions.[95,96] A p–n heterojunction of cobalt phosphide (CoP-p/NF) and nickel phosphide (NFP) supported on NF was constructed.[97] The Fermi level (EF) of CoP-p was demonstrated to be 0.76 V, while the EF of NFP was −0.15 V (Fig. 5a). When combined, a built-in potential (E_{BI}) of 0.61 V was generated, by which electrons transferred from Ni_2P to CoP to induce the hetero-interface effect. Owing to the unique band structure and electron redistribution, the as-prepared heterostructure catalyst showed outstanding bifunctional ability for SMOR and HER with both $FE_{formate}$ and $FE_{hydrogen}$ of near 100%. This research evidenced the advantage of heterostructures for organic molecule oxidation and hydrogen production. Furthermore, the local phase composition and atom arrangement at the interface were explored using Fe_2O_3/NiO-NF (Fe-NF-500) as a proof-of-concept.[98] High-angle annular dark field-scanning transmission electron microscopy (HAADF-STEM) clearly showed the interface between Fe_2O_3

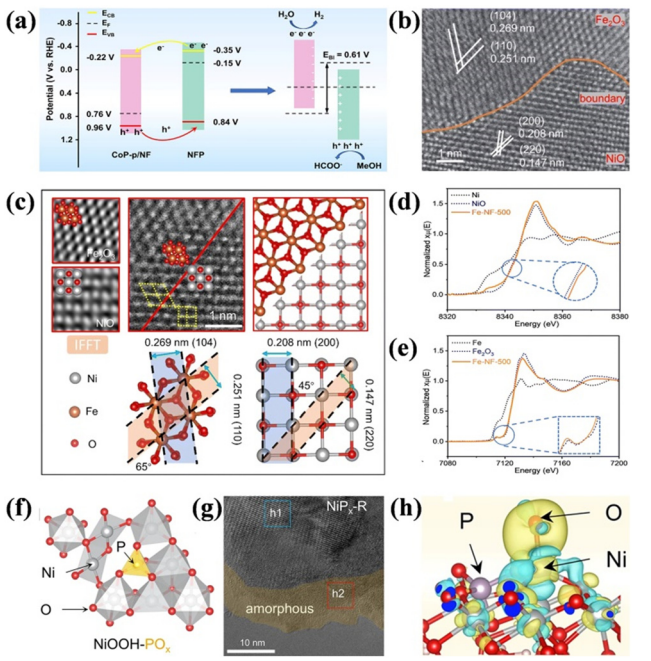

Fig. 5 (a) Energy diagrams of CoP-p and NFP before and after contact.[97] Reproduced from ref. 97 with permission from the American Chemical Society, Copyright 2023. (b) HAADF-STEM images of Fe-NF-500. (c) Atomic-resolution STEM partial enlargement images and structure analysis images. (d) Normalized XANES spectra of Ni in Fe-NF-500, NiO, and Ni foil. (e) Normalized XANES spectra of Fe in Fe-NF-500, Fe_2O_3, and Fe foil.[98] Reproduced from ref. 98 with permission from the Royal Society of Chemistry, Copyright 2023. (f) Optimized structural models of NiOOH-PO_x. (g) HRTEM image of NiP_x-R. (h) Charge density difference of OH intermediates adsorption on NiOOH-PO_x.[100] Reproduced from ref. 100 with permission from Springer Nature, Copyright 2022.

and NiO (Fig. 5b). The analysis of the atomic distribution revealed that the crystal face of Fe_2O_3 was the (110) and (104) crystal planes with a rhombic angle of 65°. In contrast, NiO had a diffraction streak angle of 45° between the (220) and (200) crystal planes (Fig. 5c). It should be noted that some dislocations may have occurred because of the mismatch of the lattice interface. The variation in the chemical valence state at the interface was also probed by X-ray absorption spectroscopy. As shown in the X-ray absorption near-edge structure (XANES) spectra of all the samples (Fig. 5d and e), the Ni K-edge absorption region of Fe-NF-500 shifted to a higher energy compared with NiO, representing an increase in the Ni valence state. In contrast, the Fe rising edge of Fe-NF-500 was slightly negatively shifted in comparison with Fe_2O_3, indicating a lower chemical valence of Fe in the heterostructure. This phenomenon demonstrated the electron flow from NiO to Fe_2O_3. The strong electronic interactions generated favorable collaborative active sites for the selective conversion from methanol to formate and inhibited its further oxidation. In addition to the electronic effect, heterostructure catalysts also can generate synergistic active centers to boost SMOR. Taking Cu_2Se/Co_3Se_4 as an example, complex species including Cu*–OOH, Co*–OOH, and SeO_x were found to coexist on its surface/interface, as proven by experimental results and DFT calculations, which synergistically modulated the adsorption/activation behavior and inhibited further oxidation to CO_2.[99] Besides the hetero-interface between crystals, a hetero-interface comprised of crystal and amorphous substances was also studied. Li *et al.* synthesized Ni-metalloid NiP_x as a pre-catalyst and obtained oxyanion-coordinated $NiOOH\text{-}PO_x$ catalysts after electrochemical oxidation (Fig. 5f).[100] The as-prepared $NiOOH\text{-}PO_x$ exhibited an obvious crystalline-amorphous interface between the NiOOH layer and Ni_2P (Fig. 5g). The charge density difference revealed the electron transfer from the oxygen atoms in OH to Ni species (Fig. 5h). This electronic effect tuned the active-center coordination environment and favored methanol transformation. As aforementioned, interfacial engineering of heterostructure construction has great potential for boosting SMOR-assisted water splitting.

3.3 Constructing dual active sites

SMOR is a four-electron process with various intermediates and possible reaction pathways. In theory, a catalyst with a single active site cannot provide the optimal conditions (activity, adsorption energy, anti-poisoning ability, *etc.*) for all the fundamental steps. Alternatively, the construction of dual active sites may ensure each step occurs at their preferred reactive site, thus accelerating the overall reaction kinetics. Furthermore, the existence of dual active sites is conducive to fabricating bifunctional catalysts for SMOR-assisted water splitting. For instance, a spinel catalyst of $NiFe_2O_4$ loaded on nickel foam ($NiFe_2O_4$/NF) was synthesized as a bifunctional catalyst for SMOR and HER.[24] DFT calculation revealed that the adsorption energy of the C1 intermediates including CO*, CH_3O*, CH_2O*, H_2COOH*, and HCOOH* on the Fe site was larger than that on the Ni site. In contrast, *OH was more strongly adsorbed on the Ni site (−3.567 eV) in relation to the Fe site (−2.431 eV) (Fig. 6a and b). This phenomenon suggested that the methanol activation preferentially occurred on the Fe site, and the Ni site was more favorable for H_2O activation. Under the action of dual active sites, a current density of more than 800 mA cm^{-2} was achieved at 2.0 V in a two-electrode system with a high $FE_{formate}$ (>95%) and $FE_{hydrogen}$ (>96%). It is known that Pt catalysts have high intrinsic activity for methanol oxidation but are vulnerable to CO poisoning.[101] Thus, a dual-site strategy was used to modify the Pt single-atom catalyst for SMOR by anchoring Pt_1 on dual-doped TiO_2 ($Pt_1/Ti_{0.8}W_{0.2}N_xO_y$).[102] Therein, the activation and dehydrogenation of CH_3O* were likely to happen on the W sites due to the lower free energy (Fig. 6c). Moreover, the resultant CHO* was transferred to the Pt_1 site for further oxidation to formate. In the meantime, the OH^- adsorbed on the W–O site favored the oxidation of the CO toxic intermediate, alleviating the poisoning effect. Finally, a high mass activity of 560 mA mg_{Pt}^{-1} at 0.82 V *vs.* RHE and formate selectivity of 90% were achieved due to the P_1–WO_{3-x} dual active sites.

The construction of dual active sites is even more crucial for acidic SMOR. Unlike alkaline media with sufficient OH^-, which is more favorable for SMOR, the acidic environment is not conducive to the progress of SMOR because only a small amount of OH^- can be obtained from the dissociation of water. In addition, the carbon monoxide pathway is more likely to occur in an acidic solution instead of the formate pathway.[104] Liu *et al.* performed innovative research in terms of the performance and mechanism of methanol-to-formate

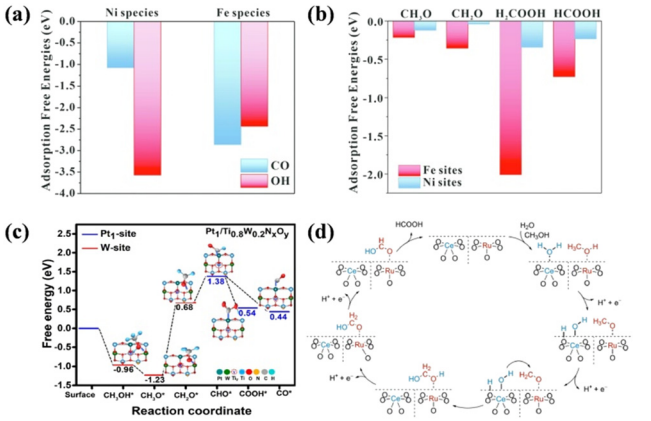

Fig. 6 (a) Adsorption energies of *OH and *CO on the surface of $NiFe_2O_4$. (b) Adsorption energies of C1 intermediates on the Fe sites and Ni sites.[24] Reproduced from ref. 24 with permission from Elsevier, Copyright 2023. (c) Theoretical free energy calculations of reaction intermediates on dual active sites of $Pt_1/Ti_{0.8}W_{0.2}N_xO_y$.[102] Reproduced from ref. 102 with permission from Elsevier, Copyright 2022. (d) Schematic illustration of reaction pathway for the SMOR to HCOOH on CeO_2/RuO_2.[103] Reproduced from ref. 103 with permission from Elsevier, Copyright 2022.

in 0.5 M H_2SO_4 solution by integrating CeO_2 with RuO_2 (CeO_2/RuO_2).[103] The presence of CeO_2 induced oxygen vacancies and accelerated water dissociation to provide OH^- for the hydration of the intermediate in the methanol oxidation process. The electronic interaction between CeO_2 and RuO_2 promoted the formation of high-valent Ru species, which were beneficial for methanol oxidation. As shown in the reaction pathway (Fig. 6d), methanol oxidation and water activation occurred at the RuO_2 site and CeO_2 site, respectively. After two successive dehydrogenation steps on the O–H and C–H bonds, the obtained HCHO* was hydrated with the nearby dissociated water molecule to generate $HCH(OH)_2^*$. The resultant $HCH(OH)_2$ further underwent two dehydrogenation processes and produced HCOOH*, which became free formate after desorption. Though the collaborative two active sites of RuO_2 and CeO_2 promoted the selective methanol oxidation in H_2SO_4 electrolyte, and the highest $FE_{formate}$ reported in this article was only 53.7%, which is much lower than that in alkaline media. Thus, more efficient modification methods should be adopted to further improve the acidic SMOR.

3.4 Increasing the available active sites

The active site is the place where the electrocatalytic reaction occurs and it only works when exposed to the electrolyte. The more available active sites, the higher the catalytic activity under similar reaction conditions. Generally, there are two ways to obtain more available active sites, namely enlarging the surface area and increasing the density of active sites. The former can be achieved by morphology engineering, while the latter can be realized by coordination tuning. Wang *et al.* fabricated N-doped carbon-supported Co/CoO grown on cobalt foam (Co–N–C/CoO/CF),[105] and the high porosity and conductive microchannels provided a large C_{dl} value of 4.50 mF cm^{-2} (specific surface area of 83.30 m^2 g^{-1}), largely exposing the Co active sites and improving the activity with 50 mA cm^{-2} at 1.309 V *vs.* RHE. A self-supporting heterostructure catalyst of $MoN/Mo_3N/NF$ was fabricated.[106] The calculated C_{dl} value for SMOR of $MoN/Ni_3N/NF$ was 43.8 mF cm^{-2}, which was higher than that of Ni_3Mo/NF (7.8 mF cm^{-2}), Ni_3N/NF (7.0 mF cm^{-2}), and NF (1.1 mF cm^{-2}). The results showed that the heterostructure can expose more active sites compared to a single component. To further expose the active sites, a core–shell nanosheet array catalyst of $NiFe_xP$@NiCo-LDH/CC was prepared.[107] The C_{dl} of $NiFe_x$-P@NiCo-LDH/CC was calculated to be 43.9 mF cm^{-2}, which is 2.6 times larger than that of NiCo-LDH (17.1 mF cm^{-2}). The increased available surface area derived from the unique morphology greatly enhanced the SMOR activity.

Regarding the coordination modulation, it is known that when the density of actives sites increases to a certain degree, the interaction within adjacent atoms or moieties cannot be ignored, which may induce better catalytic properties.[108] Thus, the design of coordination modulation is beneficial to largely increase the density of active sites. Especially for the surface atoms, they usually have a low coordination number and unsaturated bonds, which make them more chemically reactive.[109] Meanwhile, they can more readily adsorb and react with electrochemical species. In summary, the coordination number affects the ECSA by influencing the density and reactivity of the active sites. For example, 3D Mo-doped $Ni(OH)_2$ with low Ni–Ni coordination was designed.[110] DFT and X-ray absorption spectroscopy revealed that the low coordination of Ni–Ni not only increased the density of active sites but also introduced porosity, thus increasing the contact area and facilitating the catalytic reaction.

4. Catalysts and catalytic performance

To provide an intuitive overview and comparison of the catalytic performance of SMOR, nearly all the catalysts reported in the recent literature are listed in Table S1,† including their composition, electrolyte, scan rate, potential at certain current density, faradaic efficiency, and stability. It can be seen that the vast majority of research is conducted under alkaline conditions, the commonly used background solution is 1 M KOH or NaOH, and the concentration of CH_3OH ranges from 0.5 to 4 M. Some researchers used simulated seawater containing 3.5% NaCl as the electrolyte to selectively oxidize methanol. Only one study on acid SMOR was performed in 0.5 M H_2SO_4 and 2.5 M CH_3OH. The potential at a certain current density is widely regarded as the standard for comparing catalytic ability. It has been found that lowering the potential at 10 mA cm^{-2} below 1.3 V *vs.* RHE is a challenge for non-noble metal catalysts. Regarding catalytic selectivity, the faradaic efficiency of formate of most catalysts can exceed 90% and even reach close to 100%. In the following part, initially we will briefly introduce the catalytic performance descriptors, and then discuss the catalyst development in detail according to the elemental composition.

4.1 Catalytic performance descriptors

4.1.1 Activity, kinetics, and stability. The evaluation of catalytic activity, kinetics, and stability of SMOR is similar to many other electrochemical reactions such as OER and urea oxidation reaction (UOR), and the relevant concepts and calculation processes have been fully discussed elsewhere;[111,112] thus, we will not discuss them in detail and just give a brief introduction. For a catalyst, its cyclic voltammetry (CV) curve is usually recorded in 1 M KOH with and without CH_3OH of a certain concentration to probe the difference between methanol oxidation and water oxidation (Fig. 7a).[113] The comparison of methanol oxidation activity of different catalysts is implemented by scanning CV or linear sweep voltammetry (LSV) curves in alkaline methanol electrolyte (Fig. 7b).[98] The criterion is the demanded potential at a certain current density. The lower the potential, the better the catalytic ability. The commonly used current

density is 10 mA cm^{-2}, which is the predicted current density for a 10% competent solar-to-fuel conversion device under 1 sun illumination.[114,115] However, tens or hundreds of current densities are preferred nowadays to meet the demand of industrial applications.[116,117] The above-mentioned current density is the apparent/geometric current density, which means the current generated per unit area of the electrode. When the current is normalized to the electrochemical surface area (ECSA), the specific activity is obtained. The specific activity can eliminate the influence of catalyst morphology and structure, only reflecting the catalytic ability per unit active area, which can better reveal the intrinsic activity of the catalyst. There are two prevailing ways to obtain ECSA, one is calculating the double-layer capacitance (C_{dl}) from CV curves conducted with various scan rates in the non-faradaic range (Fig. 7c and d),[118] and the other is integrating the area of the reduction peak of the CV curve (Fig. 7e and f).[113] In addition, the $HCOO^-$ current density was also reported in some literature by multiplying the current density with $FE_{formate}$ to compare the net current for producing formate.[119] A detailed introduction to $FE_{formate}$ was presented in section 4.1.2.

The catalytic kinetics can be approximately estimated by the Tafel slope calculated from the CV curves and electrochemical impedance spectroscopy (EIS).[121–124] A small Tafel slope means that a smaller potential change will cause a larger increase in current density,[125] indicating fast kinetics. By fitting the EIS Nyquist plot with an equivalent circuit, the charge transfer resistance (R_{ct}) can be obtained, where the smaller the R_{ct}, the easier the reaction is to proceed. Catalytic stability is an important indicator for evaluating whether a catalyst can be put into practical use. The durability in SMOR is mainly probed by long-term steady-state stability tests using chronoamperometry (CA) or chronopotentiometry (CP) techniques and dynamic stability evaluation by consecutively scanning LSV or CV curves (Fig. 7g).[86]

The catalytic performance of a catalyst in SMOR can be explored *via* the above-mentioned tests in a three-electrode system, which is the half-reaction for SMOR-assisted water splitting. Therefore, a two-electrode system is utilized to investigate the performance of selective methanol electrolysis (Fig. 7h).[120] Therein, the as-prepared catalyst can serve as the anode or both the anode and cathode to investigate its bifunctional catalytic activity. In some reports, the absence of bubbles on the anode is considered evidence of good selectivity for methanol oxidation without oxygen evolution.[118,126] To further probe the feasibility of practical use, SMOR also can be tested in a membrane electrode assembly (MEA) (Fig. 7i).[119] Typically, MEA is assembled with an anion exchange membrane (AEM) and bipolar plate. The anolyte and catholyte are CH_3OH-containing KOH solution

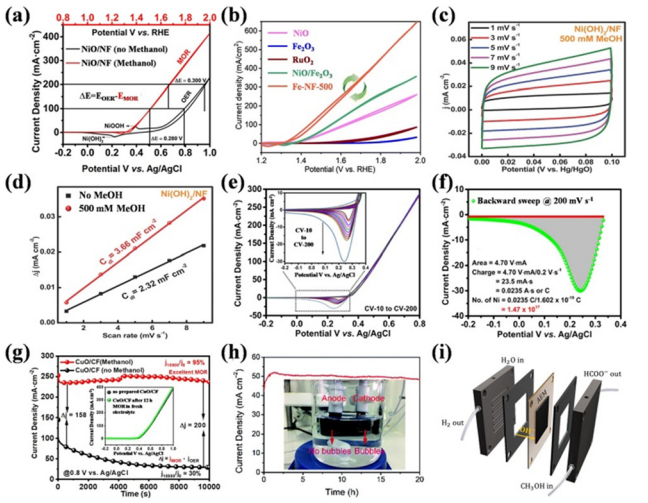

Fig. 7 (a) CV curves for NiO/NF in the presence and absence of methanol in 1.0 M KOH.[113] Reproduced from ref. 113 with permission from the American Chemical Society, Copyright 2021. (b) CV curves for all the as-prepared samples in 1.0 M KOH and 1 M CH_3OH.[98] Reproduced from ref. 98 with permission from the Royal Society of Chemistry, Copyright 2023. (c) CV curves of $Ni(OH)_2$/NF in 1.0 M KOH with MeOH at different scan rates. (d) Corresponding C_{dl} value comparison of $Ni(OH)_2$/NF in 1 M KOH with and without MeOH.[118] Reproduced from ref. 118 with permission from Elsevier, Copyright 2021. (e) CVs of NiO/NF in 1 M KOH and 1 M methanol obtained at different scan rates. (f) Scale-up of reverse CV curve of NiO/NF.[113] Reproduced from ref. 113 with permission from the American Chemical Society, Copyright 2021. (g) Chronoamperometric curves recorded in N_2-purged 1 M KOH with and without 1 M MeOH.[86] Reproduced from ref. 86 with permission from Springer Nature, Copyright 2022. (h) Stability test for the Pt–Co_3O_4/CP towards the electrocatalytic HER coupled with methanol oxidation at 1.0 V (inset is the photograph of the electrolytic cell).[120] Reproduced from ref. 120 with permission from the Royal Society of Chemistry, Copyright 2021. (i) Illustration of the MEA cell.[119] Reproduced from ref. 119 with permission from Elsevier, Copyright 2022.

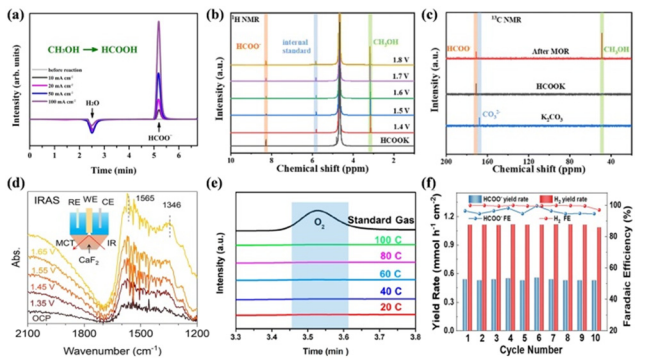

Fig. 8 (a) IC traces of the electrolyte.[127] Reproduced from ref. 127 with permission from John Wiley and Sons, Copyright 2021. (b) ^1H NMR results of the electrolyte after MOR. (c) ^{13}C NMR spectra after MOR.[56] Reproduced from ref. 56 with permission from the Royal Society of Chemistry, Copyright 2023. (d) IRAS spectra of MOR on the surface of NiP_x-R in the electrolyte of 0.1 M KOH with 0.5 M methanol.[100] Reproduced from ref. 100 with permission from Springer Nature, Copyright 2022. (e) GC traces from the anode at different passed charges at 0.6 V.[128] Reproduced from ref. 128 with permission from the American Chemical Society, Copyright 2021. (f) FE and yield rate for $HCOO^-$ and H_2 during the cycling test at 60 mA cm^{-2}.[129] Reproduced from ref. 129 with permission from John Wiley and Sons, Copyright 2023.

and pure KOH solution, respectively. Polarization curves and steady-state stability tests can be conducted to evaluate the SMOR and HER performance.

4.1.2 Selectivity. To validate the selective oxidation of methanol to formate, selectivity is a critical concern. The liquid product and probable gas product of CO_2 and O_2 after the SMOR both need to be detected. The liquid product is usually collected after a several-hour reaction at a certain potential or certain current density. Therein, $HCOO^-$ can be identified through ion chromatography (IC), nuclear magnetic resonance (NMR), and infrared reflection absorption spectroscopy (IRAS). To quantitatively detect the content of $HCOO^-$ by IC and NMR, a calibration curve should be prepared in advance. In IC, the determination time should be long enough to involve all the possible liquid products (Fig. 8a).[127] In the case of NMR, internal standards such as dimethyl sulfoxide (DMSO) must be added to report the chemical shift based on the same standard substance. Both ^1H and ^{13}C NMR spectra can be used (Fig. 8b and c).[56] In the IRAS spectrum, the peaks located at 1565 and 1346 cm^{-1} are ascribed to $HCOO^-$ (Fig. 8d).[100] Regarding the gas product, gas chromatography (GC) is employed to check whether $HCOO^-$ is overoxidized to CO_2 or the occurrence of competitive OER (Fig. 8e).[128] GC can be measured online or conducted after gas collection. After quantitatively analyzing the product, the formate production rate and faradaic efficiency can be calculated (Fig. 8f).[129] There is no unified unit for the production rate in the literature, which is usually expressed as the amount of formate produced per unit volume of electrolyte or unit mass of catalyst in one hour (mmol h^{-1} cm^{-1}, mmol L^{-1} h^{-1}, and mmol h^{-1} g_{oxide}^{-1}).[69,119,129] The faradaic efficiency of methanol to formate is calculated using the following equation:[127]

$$FE_{formate}\ (\%) = \frac{4 \times n \times F}{Q} \times 100\%$$

where 4 is the electron transfer number in SMOR, n is the amount of formate produced (mol), F is the Faraday constant (96 485 C mol^{-1}), and Q is the total charge passed (C).

4.2 Catalyst development

4.2.1 Monometallic and metal alloy catalysts. The most used monometallic catalysts for SMOR is Ni metal due to its outstanding catalytic ability and relatively lower prices compared to the other non-noble metal elements. Therein, Ni metal–organic frameworks (MOFs) supported with nickel foam (NF) have mainly been adopted as carriers owing to their porous properties and the binder-free advantage of the rigid substrate.[130] For example, a novel Ni MOF with hexamethylenetetramine as the ligand was loaded on NF (Ni-MOFs-*t*/NF) for SMOR.[131] The optimized Ni-MOFs-120/NF catalyst obtained under solvent heating temperature of 120 °C showed the best activity among the tested samples with a current density of 100 mA cm^{-2} at 1.44 V *vs.* RHE. In another work, a self-supported catalyst with Ni-MOF nanosheet arrays deposited on NF (Ni-NF-Af) was fabricated for the electrosynthesis of formate *via* methanol oxidation.[132] Benefiting from the fully exposed active sites, it only needed 1.345 V *vs.* RHE to produce a current density of 100 mA cm^{-2} with ~100% selectivity for methanol-to-formate conversion. Given that the introduction of a second metal can tune the electronic configuration to improve the catalytic activity,[133] the doping strategy was utilized to modify Ni MOF. An Ir-doped Ni MOF with two types of ligands (1,4-benzenedicarboxylic acid and triethylenediamine) grown on NF (NiIr-MOF/NF) was synthesized as a bifunctional catalyst for SMOR and HER.[134] The enhanced catalytic activity and selectivity (close to 100%) were attributed to the structural and compositional advantages. The Ni MOF nanosheet arrays endowed the catalyst with efficient available active sites. Meanwhile, the incorporation of Ir modulated the electronic structure of Ni, which led to the appropriate adsorption energy for methanol and intermediates.

Compared with the single metal catalyst, metal alloys containing different metallic elements usually yield intriguing physicochemical properties such as improved conductivity and variable valence state.[135] When alloys are formed, the redistribution of electrons will occur owing to the different chemical properties of multi-components, which can lower the energy barrier for the generation of intermediates on the active sites.[136] The most commonly used elements in metal alloy catalysts for SMOR are Ni, Co, Cu, and Mo. A porous NiCo alloy with oxygen vacancies supported on NF (O_v–NiCo@NF) was used methanol upgradation.[137] The bimetallic synergism and the formation of O_v were believed to alter the electron distribution of Ni–Co, resulting in the optimum chemisorption energy of intermediates during the SMOR process. Moreover, the metallic porous structure was conducive to the penetration of the electrolyte and release of gaseous products, which accelerated the reaction kinetics. Finally, enhanced activity in SMOR-assisted hydrogen production was achieved. Only a cell voltage of 1.49 V was required to reach the current density of 50 mA cm^{-2}. Likewise, an NiCu interconnected porous nanostructure was prepared for SMOR *via* the hydrogen bubble templating electrodeposition method.[138] The insertion of Cu into Ni was claimed to improve the electronic conduction and charge transfer ability. The sacrificial template method of bubble-assisted electrodeposition enlarged the active surface area and enhanced the contact between the electrolyte and active sites, thereby promoting the hybrid electrolysis of SMOR and HER with a low cell voltage of 1.45 V at 10 mA cm^{-2}. In addition to binary alloys, ternary alloys have also been studied. Chen *et al.* fabricated NiCoMo alloy arrays on carbon cloth (NiCoMo/CC) with a nanowire/nanosheet morphology by combined the hydrothermal and annealing methods for methanol–water co-electrolysis.[139] Under the catalysis of NiCoMo/CC, the input cell voltage decreased by 208 mV by replacing OER with SMOR. Meanwhile, the $FE_{formate}$ remained above 85% after

the 50 h long-term stability test. The authors proved that Mo not only acted as an electronic structure modulator but also played the role of surface reconstruction promoter. At the anode where a positive bias was applied, substantial Mo was leached, and the residual amount of Mo was substituted in NiCoOOH, which promoted the formation of high-valent Ni^{3+}/Co^{3+} active species and optimized the adsorption/desorption energy for the intermediates. Besides binary and ternary metal alloys, high-entropy alloys have become a research hot-spot, which may be useful for SMOR in the future.[140]

4.2.2 Oxide and hydroxide catalysts. The high-valent transition metal species are recognized as active phases for organic small molecule oxidation reactions including methanol oxidation.[141,142] Thus, oxide and hydroxide, which are more prone to generate active species with high-valence states, usually generate more favorable catalytic performances.[143] An NiO nanosheet array on NF (NiO/NF) was reported to have enhanced SMOR activity with the current density of 100 mA cm^{-2} at the potential of 1.53 V *vs.* RHE.[113] The as-prepared NiO/NF also possessed the property of CO-poisoning resistance and exhibited a current retention of ~100% after a 20 000 s durability test. Another study introduced oxygen vacancies (V_o) in Co_3O_{4-x}/NF to improve SMOR.[144] Initially, the authors electrodeposited $Co(OH)_2$ on NF, and then conducted O_2 plasma and air calcination to synthesize the target Co_3O_{4-x}/NF-P and its counterpart of Co_3O_4/NF-C, respectively. The V_o-enriched Co_3O_{4-x}/NF-P merely needed 1.318 V *vs.* RHE to deliver 10 mA cm^{-2} in SMOR. When coupled with HER, the cell voltage at 10 mA cm^{-2} for methanol-assisted water splitting was only 1.540 V. The experimental and calculation results demonstrated that the V_o promoted the phase transformation of Co_3O_{4-x}/NF-P, which accelerated the deprotonation of methanol and suppressed the further oxidation of HCOO*. Therefore, the FE of methanol to formate exceeded 95% at the passed charges from 50 to 250 C. Furthermore, copper oxide was also proven to be efficient for SMOR. Wei *et al.* used CuO nanosheets grown on copper foam (CuO NS/CF) as an anodic catalyst for methanol oxidation.[8] The largest $FE_{formate}$ of CuO NS/CF for SMOR reached 97% and an ultra-low potential of 1.47 V *vs.* RHE at 100 mA cm^{-2} was achieved. Besides the commonly used first-row 3d transition metal oxides, amorphous Nb_2O_5 was reported as a new type of electrocatalyst for methanol electro-reforming.[145] *In situ* Raman revealed that the short Nb–O bond in the amorphous structure was the origin of the enhanced activity, and a near 100% of $FE_{formate}$ was obtained. Perovskite is a type of mixed oxide used in many catalytic reactions due to its low cost, diversity of element composition, and the outstanding properties of being substituted and doped.[146,147] An iron-substituted lanthanum cobaltite ($LaCo_{1-x}Fe_xO_3$) was employed to realize the mild oxidation of methanol to formate.[119] The catalytic performance was optimized by tuning the Fe/Co ratio, and $LaCo_{0.5}Fe_{0.5}O_3$ was found to have the highest formate production rate of 24.5 mmol h^{-1} g_{oxide}^{-1}.

Hydroxide is the most studied catalyst for SMOR owing to its simple synthesis, facile active phase formation, and high intrinsic activity. To date, $Ni(OH)_2$, NiCo-LDH, NiFe-LDH, and their derivatives have been developed. The pure phase of $Ni(OH)_2$ on NF can be employed as a bifunctional catalyst for SMOR and HER *via* a simple hydrothermal or ultrasonic synthesis process.[118,148] Its activity can be further improved by the cation doping strategy. Ming *et al.* prepared Co^{2+}-doped $Ni(OH)_2$ nanosheets on NF *via* the facile electrodeposition approach.[149] The optimal catalyst with the Co^{2+} doping content of 10 mol% exhibited the best activity with 1.32 V *vs.* RHE at 100 mA cm^{-2}. The $FE_{formate}$ was improved to above 96.5%. Moreover, doping chromium into α-$Ni(OH)_2$ was also reported to realize the efficient selective conversion of methanol to formate.[150] The Cr dopant increased the conductivity of $Ni(OH)_2$, accelerated the adsorption of methanol, and optimized the kinetics for the formation of NiOOH, thereby achieving a faradaic efficiency of 92.1% for formate. Unlike the single hydroxide with one metal cation, LDHs are comprised layers of divalent and trivalent metal cations coordinated to hydroxide anions and the intercalated charge compensating anions between metal layers.[151,152] Because of their flexible chemical composition and exchangeable interlaminar anions, LDHs display attractive electrocatalytic performances.[153] For example, Ni_x-$Co_{1-x}(OH)_2$/NF was reported to have approximately 100% $FE_{formate}$ and the optimal $Ni_{0.33}Co_{0.67}(OH)_2$/NF catalyst displayed the highest activity and robustness for the co-

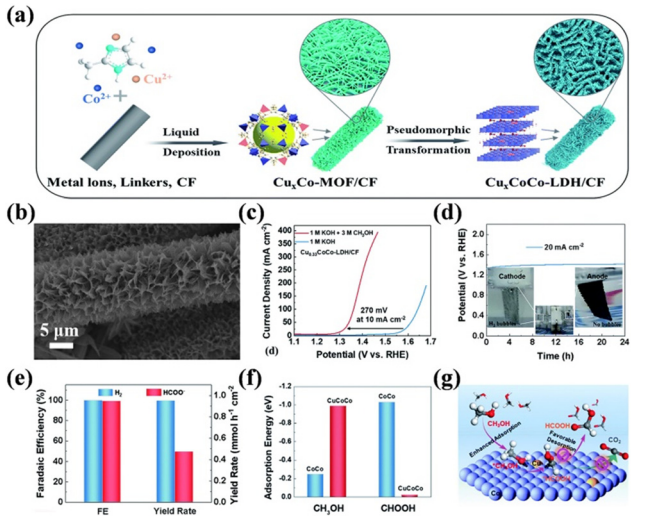

Fig. 9 (a) Schematic illustration of the fabrication of Cu_xCoCo-LDHs/CF. (b) SEM image of $Cu_{0.33}CoCo$-LDHs/CF. (c) Polarization curves of $Cu_{0.33}CoCo$-LDH/CF in 1 M KOH or 1 M KOH + 3 M CH_3OH solution. (d) Chronopotentiometry curve of $Cu_{0.33}CoCo$-LDH/CF in 1 M KOH + 3 M CH_3OH solution at 20 mA cm^{-2}. (e) Comparison of the FE and yield rate for formate and H_2 on $Cu_{0.33}CoCo$-LDH/CF. (f) Calculated adsorption energy of methanol and formate molecules on the surfaces of CoCo-LDH and CuCoCo-LDH. (g) Schematic process for the transformation of CH_3OH molecules into HCOOH instead of CO_2 on the surface of CuCoCo-LDH.[154] Reproduced from ref. 154 with permission from the Royal Society of Chemistry, Copyright 2022.

generation of formate and H_2 *via* the assistance of SMOR.[126] In another study, Liu *et al.* incorporated Cu^{2+} in Co LDH to obtain a novel SMOR catalyst (Cu_xCoCo-LDHs/CF) with an interconnected nanosheet array morphology through the combined method of liquid deposition and pseudomorphic transformation (Fig. 9a and b).[154] In the anodic reaction, $Cu_{0.33}$CoCo-LDHs/CF yielded a current density of 10 mA cm^{-2} at 1.28 V *vs.* RHE for SMOR, which was 270 mV lower than that of OER (Fig. 9c). When coupling SMOR with HER, the catalyst could stably run for 24 h and no bubbles were observed on the anode electrode (Fig. 9d). The $FE_{formate}$ and $FE_{hydrogen}$ both reached about 99% (Fig. 9e). DFT calculations revealed that the adsorption energy of HCOOH on CuCoCo-LDH (−0.023 eV) was lower than that of CoCo-LDH (−1.03 eV) (Fig. 9f), which accelerated the desorption of HCOOH, avoiding its over-oxidation and increasing the selectivity (Fig. 9g).

4.2.3 Non-metal alloy catalysts. Non-metal alloys refer to the alloying of metal elements and non-metal elements. They have been widely studied due to their reasonable cost, convenient preparation, and diverse electronic structures. The size of the non-metallic anion, the geometric structure, bonding energy, and coordination number of non-metal alloys can all be tuned to optimize their catalytic performance.[155] More importantly, the various valance states of non-metal elements are beneficial for the surface reconstruction and phase transition of the catalyst to achieve desirable activity.

Metal carbides have been reported to have the superiority of flexibility, anisotropy, excellent conductivity, and chemical stability.[156] In 2020, Cui's group first proved the feasibility of using the non-precious metal catalyst Ni_3C for SMOR to realize near 100% $FE_{formate}$.[157] They utilized *in situ* infrared spectroscopy and NMR to identify the adsorbed and dissolved intermediates/products, and no CO adsorption and carbonate production were found, which confirmed the extremely high selectivity. Metal nitrides, acting as interstitial compounds, exhibit the characteristics of covalent compounds, ionic crystals, and transition metals because of the integration of N atoms into the parent metal atoms.[158] Meanwhile, the lattice parameter and d-band of the metal element can be modulated to generate good electrocatalytic performances.[159,160] For instance, Cu_3N nanosheets were fabricated *via* the nitridation of a Cu-containing precursor (Fig. 10a).[161] Benefiting from the surface reconstruction of Cu_3N, an $FE_{formate}$ of over 90% was obtained in the wide potential window of 1.4 to 1.8 V *vs.* RHE (Fig. 10b). In the X-ray absorption near-edge structure (XANES) profiles, the edge position of the used Cu_3N was located at a higher energy value than that of the fresh Cu_3N (Fig. 10c), indicating the formation of high-valent Cu species. In the meantime, the coordination number of Cu–O/N was revealed to increase, whereas the Cu–Cu coordination number decreased, representing the partial oxidation of the Cu_3N surface (Fig. 10d). HRTEM demonstrated the existence of an interface between the CuO layer and Cu_3N (Fig. 10e). *In situ* Raman

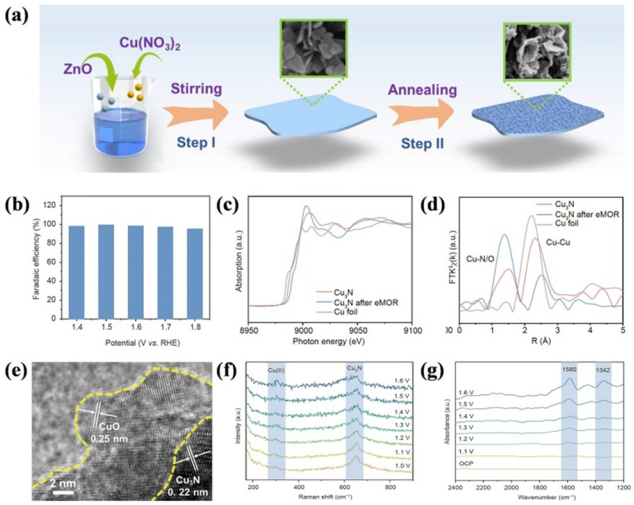

Fig. 10 (a) Schematic of the synthesis of Cu_3N nanosheets. (b) FE of Cu_3N for selective methanol conversion reactions. (c) XANES profiles and (d) FT-EXAFS spectra of Cu foil, Cu_3N, and Cu_3N after eMOR. (e) HRTEM image of Cu_3N after the reaction. (f) *In situ* Raman spectroscopy and (g) *in situ* IRAS of Cu_3N electrode.[161] Reproduced from ref. 161 with permission from Springer Nature, Copyright 2023.

detected the generation of a vibrational mode belonging to CuO with an increase in the potential during the SMOR (Fig. 10f). Moreover, *in situ* infrared spectroscopy (IR) confirmed the symmetric and antisymmetric stretching vibration of OCO in formate (Fig. 10g). All the aforementioned results evidenced that Cu_3N underwent surface reconstruction with the formation of a Cu(II) shell as the active face and the Cu_3N core ensuring electron transport. Metal phosphides have been extensively used as catalysts in various electrocatalytic reactions owing to their semiconducting property, diverse phase structure, and high activity.[162–164] In the case of SMOR, an Os-doped Ni_xP/N-doped carbon composite on NF (Os–Ni_xP/N–C/NF) was assembled to simultaneously harvest value-added formate and H_2.[165] The $FE_{formate}$ and $FE_{hydrogen}$ reached 92% and 100%, respectively. A cell voltage of 1.43 V was required to produce 10 mA cm^{-2} in alkaline methanol electrolysis. Amorphous phosphide was also investigated for SMOR. An amorphous of Ni–Co–Fe ternary phosphide ($Ni_xCo_yFe_z$–Ps) was obtained *via* the electrodeposition method.[166] $Ni_2Co_2Fe_1$–P was screened as the most suitable catalyst for SMOR. Under the catalysis of $Ni_2Co_2Fe_1$–P, the cell voltage was reduced by 110 mV to deliver 20 mA cm^{-2} by combining SMOR-HER compared to conventional water splitting.

Metal chalcogenides are a significant category of catalysts that have been widely studied. Among them, metal sulfides have attracted significant attention on account of its suitable band gap and adjustable electronic structures.[167] Taking NiS as an example, the presence of S was found to greatly influence the electronic properties of the *in situ*-formed NiOOH species, which improved the electroconductivity and accelerated the electron transfer, thereby boosting the SMOR performance.[168] The valence electron states and spin of the d

electrons of metal sulfides were also proven to be significant. Fu's group electrodeposited $NiCo_2S_4$ on carbon cloth ($CC@NiCo_2S_4$) as a bifunctional catalyst for energy-methanol hybrid electrolysis.[169] A high current density and long-term stability were achieved by modulating the magnetism on the surface of $CC@NiCo_2S_4$. XANES revealed a positive shift in the absorption edge of the used $CC@NiCo_2S_4$, indicating a reduction in the electron density of the Ni species after the reaction (Fig. 11a). Moreover, the local atomic structures involving bond length and type of the catalyst were probed through extended X-ray absorption fine structure (EXAFS) (Fig. 11b) and wavelet transform EXAFS (WT-EXAFS) spectra (Fig. 11c–f). The results proved that partial oxidation occurred on the catalyst surface. DFT calculations confirmed that the d electrons in Ni(II) and Co(III) of the fresh catalyst were all in the state of low spin (Fig. 11g). However, when adsorbed with OH, the surface Ni and Co turned into high spins with the bulk Ni and Co maintaining low spins (Fig. 11h and i). This change in spin state contributed to the enhancement in SMOR activity. Metal selenides possess similar characteristics to the corresponding metal sulfides, but display higher electron transfer ability and a lower band gap.[170,171] Se atoms are inclined to form strong covalent bonds with metal atoms,[172] thus enhancing the metallic property and resulting in a unique band structure, which favors the SMOR catalytic activity.[173,174] For example, $Ni_{0.75}Fe_{0.25}Se_2$ could generate 0.47 mmol cm^{-2} h^{-1} of formate with an $FE_{formate}$ of 99% due to its large ECSA, fast electron transfer kinetics, and high proton diffusivity.[175]

4.2.4 Heterostructure catalysts. In recent years, heterostructure catalysts have attracted increasing attention and become a hotspot of research.[176–178] Numerous studies claimed that the hetero-interface formed between different components can induce favorable properties including electron redistribution, charge transfer acceleration, adsorption energy optimization, and increase in the number of active sites.[179–182] For example, a Pt/Pd hetero-metallene catalyst was found to be efficient for methanol-assisted hydrogen evolution.[183] The heterointerface between Pt and Pd induced strong metal–metal interaction and optimized the adsorption and activation of methanol molecules in the electrocatalytic reaction. Finally, a good hydrogen evolution performance was obtained. However, heterostructure catalysts are usually confused with hybrid catalysts. Here, the heterostructure catalysts are defined as catalysts with a clear interface between two or more crystal faces of different substances.

In SMOR, phosphide- and hydroxide-based heterostructure catalysts are the most studied. For instance, a heterostructure Ni_2P-CoP/NF catalyst was prepared *via* a successive

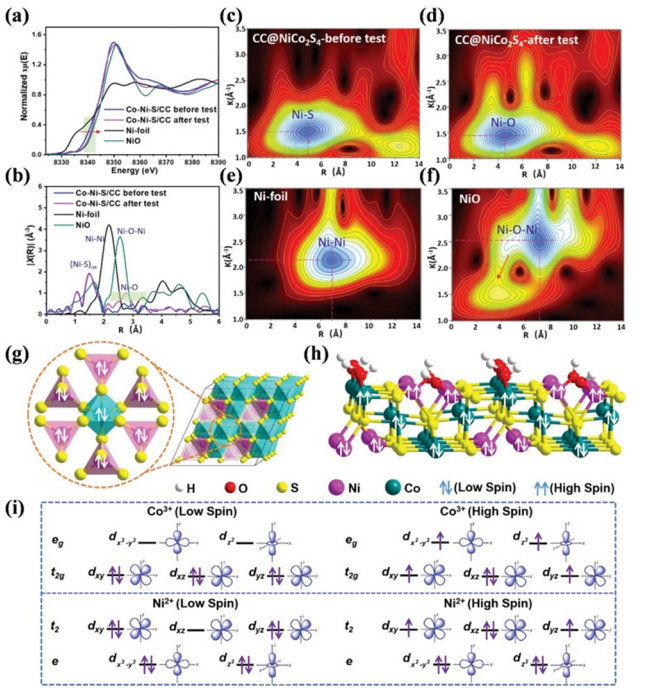

Fig. 11 (a) Ni K-edge XANES spectra of fresh $CC@NiCo_2S_4$, used $CC@NiCo_2S_4$, pristine Ni foil, and NiO. (b) Fourier transformation of the EXAFS spectra in R space. WT-EXAFS for (c) $CC@NiCo_2S_4$-before the test, (d) $CC@NiCo_2S_4$ after the test, (e) pristine Ni foil, and (f) NiO. (g) Illustration of spin for the crystalline structure of $NiCo_2S_4$. (h) Illustration of the spin of $NiCo_2S_4$. (i) Occupation of d electrons for the high-spin and low-spin Ni^{2+} and Co^{3+}, respectively.[169] Reproduced from ref. 169 with permission from John Wiley and Sons, Copyright 2022.

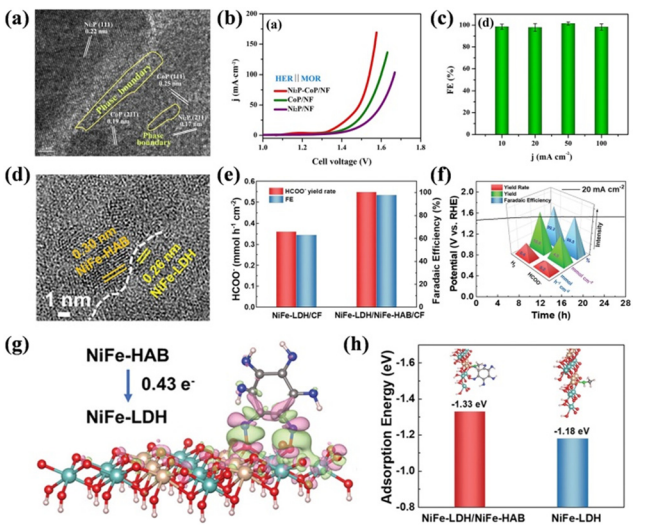

Fig. 12 (a) HRTEM image of Ni_2P–CoP/NF. (b) Cell LSV curve comparison of MOR||HER for the phosphide samples. (c) Corresponding FE of formate at current densities of 10, 20, 50, and 100 mA cm^{-2}.[127] Reproduced from ref. 127 with permission from John Wiley and Sons, Copyright 2021. (d) HRTEM images of NiFe-LDH/NiFe-HAB/CF. (e) Comparison of FE and yield rate for formate on NiFe-LDH/CF and NiFe-LDH/NiFe-HAB/CF. (f) Chronopotentiometry curve at 20 mA cm^{-2}, FE, yield, and yield rate for H_2 and $HCOO^-$ on NiFe-LDH/NiFe-HAB/CF. (g) Differential charge density image of NiFe-LDH/NiFe-HAB/CF. (h) Adsorption energy of methanol on the surfaces of NiFe-LDH and NiFe-LDH/NiFe-HAB.[129] Reproduced from ref. 129 with permission from John Wiley and Sons, Copyright 2023.

electrodeposition and phosphidation method.[127] An obvious phase boundary was observed between Ni_2P and CoP, which induced an interfacial bonding effect and exposed more active area (Fig. 12a). When used as a bifunctional catalyst in the two-electrode system, Ni_2P-CoP/NF delivered 10 mA cm^{-2} at a cell voltage of 1.35 V (Fig. 12b). Meanwhile, an $FE_{formate}$ of 100% was achieved at the given current densities (Fig. 12c). In the case of hydroxide-based heterostructure catalysts, a core–shell structured $Cu(OH)_2$@$NiFe(OH)_x$ catalyst was built *via* a facile ion exchange method.[128] The heterointerface induced a strong synergistic effect due to the hydroxide and optimized the adsorption energy for the reactants and intermediates, thereby improving the SMOR performance. In another study, NiFe-LDH was assembled on an SnO_2 supported NF layer by layer (NiFe LDH@SnO_2/NF).[184] The semiconductor SnO_2 layer not only regulated the growth of NiFe-LDH but also altered the electron distribution around the interface, leading to an increase in the valence state of Fe and Ni. The SnO_2 layer also acted as an electron transport layer, which accelerated the electron transfer from NiFe-LDH to the NF electrode. Due to these properties, enhanced SMOR activity was obtained. It is known that there exists a competition zone of MOR and OER in the conventional OER potential window, thus suppressing OER is beneficial to maintain efficient MOR. To achieve this goal, the strategy of constructing heterostructure catalysts has been employed. As reported, heterostructure NiFe-LDH and NiFe-hexylaminobenzene loaded on carbon fibers (NiFe-LDH/NiFe-HAB/CF) exhibited near 100% of $FE_{formate}$ with the suppression of OER activity (Fig. 12d–f).[129] DFT calculations revealed that 0.43 e^- transferred from NiFe-HAB to NiFe-LDH across the interface (Fig. 12g), leading to the NiFe-HAB being a passivation layer for OER. Moreover, the adsorption energy value of methanol molecules on NiFe-LDH/NiFe-HAB/CF was found to be more negative than that on NiFe-LDH (Fig. 12h), indicating the favorable methanol adsorption and activation, which significantly improved the activity and selectivity of SMOR. The heterostructure composed of phosphide and hydroxide was also proven to be efficient for selective methanol oxidation. Fu's group coated NiCo-LDH on Co_xP nanosheet arrays to build a heterostructure catalyst (Co_xP/NiCo-LDH).[185] The ultrathin NiCo-LDH provided a large electrochemical active area and Co_xP endowed the catalyst with fast charge transfer at the interface. Therefore, enhanced catalytic activity, kinetics, and stability were achieved. Similarly, a heterostructure catalyst assembled by binary metal phosphides $NiCo_xP$ and NiCo-LDH also showed an improved SMOR performance due to the synergism of the two hetero-components.[186]

4.2.5 Hybrid catalysts. Both hybrid and heterostructure catalysts contain multiple components, but unlike heterostructures, which mainly exhibit electronic effect, hybrid catalysts without clear hetero-interfaces usually yield a synergistic effect. The synergistic effect is a relatively broad concept referring to the combination of advantages of various components in a catalyst,[187,188] which compensate for their individual weakness and jointly improve the catalytic performance. A combination of Pt and Co_3O_4 assembled on carbon paper (Pt–Co_3O_4/CP) showed brilliant bifunctional catalytic properties for SMOR and HER.[120] An ultralow cell voltage of 0.555 V was required to deliver 10 mA cm^{-2}, which is 1022 mV smaller than that of water splitting. It can be seen that combining noble metals with non-precious metals to form a hybrid catalyst can reduce the energy input, and simultaneously maintain their activity as much as possible. Similarly, the strategy of fabricating single-atom catalysts (SACs) can also maximize the catalytic activity by minimizing the amount of catalyst. For example, Ahmad *et al.* synthesized PtRu SACs on N-doped porous carbon to co-produce electricity and formate in DMFC, which can be adopted in the preparation of catalysts for methanol–water hybrid electrolysis.[189] In addition to the compositional modulation, the catalytic activity of a hybrid catalyst can also be enhanced by creating dual active sites and morphology engineering. For example, in a hybrid catalyst of Ru&Fe–WO_x, the synergism of WO_x and Ru&Fe adjusted the H* adsorption on the *in situ*-formed lattice oxygen and HCOO* desorption on the Ru site.[190] Meanwhile, the interconnected hierarchical morphology enhanced the mass transfer and improved the catalytic durability. Finally, a high current density of 500 mA cm^{-2} was obtained at the low cell voltage of 1.62 V with both $FE_{formate}$ and $FE_{hydrogen}$ reaching approximately 100%. In another report, a core–shell catalyst of CuS@CuO/copper foam (CuS@CuO/CF) was prepared.[191] The CuO shell catalyzed methanol oxidation directly, and the subsurface CuS was believed to not only create O defects to improve the methanol adsorption and charge transfer but also suppress the further oxidation of formate. Finally, an $FE_{formate}$ of almost 100% was obtained. It should be noted that the components of the above-mentioned hybrid catalysts were all formed and well defined in the fresh catalyst. However, some hybridized components were *in situ* generated during the chemical test. Taking the NiCo alloy as an example, NiCo-NF was used as an anode catalyst for SMOR.[192] After the treatment of electrochemical conversion, stacked Ni/$Co(OH)_2$ nanolayers were formed, which possessed an excellent performance for SMOR. The resultant catalyst reached the current density of 100 mA cm^{-2} at 1.291 V with the $FE_{formate}$ approaching 100%. In Ni/WC hybrid nanoparticles, the WC and the *in situ*-formed NiOOH could activate the different functional groups of methanol and promote SMOR.[193]

5. Conclusions and perspective

Coupling water electrolysis with selective methanol oxidation is an efficient energy conversion strategy to simultaneously obtain value-added formate and green hydrogen. It not only lowers the overpotential but also harvests valuable chemicals at both the anode and cathode, which is superior to conventional water splitting. Here, we reviewed the recent advances in the electrocatalysts for selective methanol oxidation for the co-production of value-added formate and

green hydrogen, aiming to inspire more advanced research. In this work, the mechanism of SMOR was introduced and the catalyst design strategy was discussed in terms of chemical bond adjustment, electronic structure tuning, construction of dual active sites, and exposure of active sites. Then, the catalytic performance descriptors and catalyst development were summarized. It was demonstrated that noble metals tend to completely oxidize methanol to CO_2, while non-noble metals are more favorable to SMOR due to their moderate activity. The active sites of non-noble metals are widely recognized as the *in situ*-formed high-valent species originating from surface reconstruction. Hydroxide-based catalysts are the most extensively studied due to their easy fabrication, facile active phase formation, and high feasibility of being modified. The reaction routine mainly follows the surface adsorption mechanism (SAM) or lattice oxygen participation mechanism (LOM). By activating or inhibiting the chemical bond of methanol molecules, the process of methanol oxidation can be well controlled at the stage of formate. The strategies of foreign atom doping, defect creation, and heterostructure construction can all tune the electronic distribution of catalysts, thereby optimizing the adsorption/desorption energy of the reactants/intermediates and reducing the energy barrier. Constructing dual active sites can greatly improve the bifunctional ability of methanol electrolysis, especially in acid media. Increasing the available active sites may enlarge the electrochemical surface area and expose more active sites, hence improving the activity.

However, although many momentous discoveries and remarkable progress have been achieved in improving SMOR, there are still some ambiguities, restrictions, and challenges that need to be addressed.

(1) Mechanism study: (i) it is known that dehydrogenation can occur on two sites of the methanol molecule (C–H bond or O–H bond) at the initial stage. Thus, it is necessary to identify which path SMOR follows based on more direct and convincing evidence. (ii) The prevailing mechanisms used to analyze SMOR nowadays are the adsorption mechanism and lattice oxygen mechanism, and the *in situ*-formed NiOOH is commonly regarded as the real active phase. Actually, the conclusion of the active sites being Ni^{3+} species derived from surface reconstruction in many electrocatalytic reactions was raised many years ago and has been adopted to date. Attractively, in recent years, some new mechanisms have been proposed for OER and UOR, which share the same high-valent active Ni species with methanol oxidation. In the case of OER, the new mechanism of light-triggered coupled oxygen evolution mechanism (COM) and oxide path mechanism (OPM) was proposed.[194,195] Regarding UOR, the active site of Ni^{4+} species and a new two-stage reaction pathway involving ammonia formation and its subsequent oxidation to N_2 was revealed, which is different from most other Ni-based catalysts with NiOOH as the active phase.[196,197] Therefore, more in-depth study is needed to determine whether there are other mechanisms involved in SMOR to make a breakthrough. (iii) In addition to pure Ni-based catalysts, other catalysts with multi-component metallic compounds including Ni element have also been reported to possess high-valent Ni species as the active sites. The valence state and role of other metals should also be explored. (iv) An increasing number of reports on heterostructure catalysts attributed the enhanced SMOR performance to the *in situ*-formed hetero-interface. However, the investigation of hetero-interfaces is mostly a qualitative description, lacking quantitative insight. Thus, more quantitative properties of hetero-interfaces should be identified to better understand the catalytic mechanism, such as the crystal phase composition, lattice distortion, interface length, spacing, and area, the origin of heterostructure catalyst activity, and surface structure evolution. (v) Although the overpotential of SMOR is lower than that of OER, there still exists a certain competitive relationship between them. Specifically, two types of oxidation currents coexist within a certain potential window. Therefore, identifying the cross-competition region and determining the origin of the current are significant to optimize the potential window and promote the understanding of the anode coupling process in hybrid water electrolysis. (vi) DFT calculations and *in situ* characterizations have been widely used to probe the catalytic mechanism. However, it is difficult to simulate the changes in the external conditions in catalytic reactions, such as the electrolyte concentration and mass transfer, *via* DFT. *In situ* characterizations have their own limitation and application range. Thus, machine learning can be a good supplement by building models from data to better understand the structure–activity relationship.

(2) Performance evaluation: (i) selectivity is the most significant descriptor to evaluate the SMOR activity. Generally, the selectivity of methanol to formate is described by FE. A few studies calculated the production rate of formate. Nevertheless, the conversion rate of formate is rarely mentioned in the literature. Thus, it is suggested to detect the consumption of methanol to examine the conversion rate of formate. (ii) It is known that 100% of FE means all the input electrons are devoted to generating the corresponding product. Thus, an FE below 100% indicates there are byproducts generated. However, lots of reports on FE below 100% did not explain whether any other byproducts exists. Thus, this issue should be further addressed. (iii) Stability is an indispensable concern in practical use. Thus far, the main durability evaluation method used is the steady-state stability test by conducting CA and CP measurements for tens of hours. The dynamic stability evaluation by comparing the CV or LSV curves before and after cycling tests will be an important supplement to catalytic stability. Moreover, the time for the stability test should be further extended to estimate the potential of practical use. (iv) Moreover, the change in the morphology, structure, and element composition of the catalyst during electrocatalysis should also be given attention. They are significant in the study of

surface reconstruction, catalyst degradation, and inactivation mechanism.

(3) Large-scale production and practical application. (i) Restricted by the experimental instrument size and precise operation, the catalysts prepared in the laboratory have a small scale with several mg or g. Alternatively, their large-scale synthesis may lead to the problem of unevenness and instability. Thus, techniques for the scaled-up fabrication of catalysts that balance activity and stability should be developed for practical application. (ii) It can be seen that the electrochemical tests of SMOR and SMOR&HER were nearly all conducted in three-electrode or two-electrode systems throughout the literature. Few reports implemented SMOR in MEA, which is more closely related to the actual working conditions. Loading catalysts and evaluating their performance in MEA can explore the feasibility of practical applications and provide a scientific basis for engineering amplification. (iii) A critical issue that must be considered is how to collect the produced formate. Formate and methanol are both liquids, and thus certain separation techniques must be used to extract formic acid. Also, the difficulty and cost of the post-treatment should be appraised.

Data availability

No primary research results, software or code has been included and no new data were generated or analysed as part of this review.

Conflicts of interest

There are no conflicts to declare.

Acknowledgements

This work is financially supported by the National Natural Science Foundation of China (22090030).

References

1 H. Zhang, Y. Fu, H. T. Nguyen, B. Fox, J. H. Lee, A. K. Lau, H. Zheng, H. Lin, T. Ma and B. Jia, *Coord. Chem. Rev.*, 2023, **494**, 215272.
2 J. Na, H. Yu, S. Jia, J. Chi, K. Lv, T. Li, Y. Zhao, Y. Zhao, H. Zhang and Z. Shao, *J. Energy Chem.*, 2024, **91**, 370–382.
3 L. Ding, Y. Zhang, T. Wang, P. Li and K. Chang, *Catal. Sci. Technol.*, 2024, **14**, 1730–1755.
4 Y. Kuang, R. He, X. Gu, F. Yang, X. Tian and L. Feng, *Chem. Eng. J.*, 2023, **456**, 141055.
5 Y. Tsubonouchi, Z. N. Zahran, D. Chandra, N. Hoshino and M. Yagi, *Catal. Sci. Technol.*, 2024, **14**, 3287–3319.
6 W. Zhu, Z. Yue, W. Zhang, N. Hu, Z. Luo, M. Ren, Z. Xu, Z. Wei, Y. Suo and J. Wang, *J. Mater. Chem. A*, 2018, **6**, 4346–4353.
7 A. Shankar, S. Marimuthu and G. Maduraiveeran, *J. Mater. Chem. A*, 2024, **12**, 121–127.
8 X. Wei, Y. Li, L. Chen and J. Shi, *Angew. Chem., Int. Ed.*, 2021, **60**, 3148–3155.
9 Y. Aykut and A. Bayrakçeken Yurtcan, *Electrochim. Acta*, 2023, **471**, 143335.
10 H. Wang, Q. Hu, J. Qiu, R. Guo and X. Liu, *Catal. Sci. Technol.*, 2023, **13**, 6102–6125.
11 Z. Li, L. Sun, Y. Zhang, Y. Han, W. Zhuang, L. Tian and W. Tan, *Coord. Chem. Rev.*, 2024, **510**, 215837.
12 E. Lee, J. H. Kim, J. Choi, Y. Hong, D. Shin, H. Yun, J. Kim, G. Bak, S. Hong and Y. J. Hwang, *J. Mater. Chem. A*, 2023, **11**, 16559–16569.
13 J. Li, S. Sun, Y. Yang, Y. Dai, B. Zhang and L. Feng, *Chem. Commun.*, 2022, **58**, 9552–9555.
14 F. Arshad, T. u. Haq, I. Hussain and F. Sher, *ACS Appl. Energy Mater.*, 2021, **4**, 8685–8701.
15 L. Yu, X. Pang, Z. Tian, S. Wang and L. Feng, *Electrochim. Acta*, 2023, **440**, 141724.
16 T. V. M. Sreekanth, K. Prasad, J. Yoo, J. Kim and K. Yoo, *Catal. Sci. Technol.*, 2023, **13**, 3445–3455.
17 T. Wang, X. Cao and L. Jiao, *Angew. Chem., Int. Ed.*, 2022, **61**, e202213328.
18 Q. Qian, Y. Zhu, N. Ahmad, Y. Feng, H. Zhang, M. Cheng, H. Liu, C. Xiao, G. Zhang and Y. Xie, *Adv. Mater.*, 2024, **36**, 2306108.
19 K. Lu, Y. Zhang, Y. Shen and H. Li, *Catal. Sci. Technol.*, 2024, **14**, 2973–2990.
20 K. Yan, Y. Liu, Y. Lu, J. Chai and L. Sun, *Catal. Sci. Technol.*, 2017, **7**, 1622–1645.
21 W. Zhang, Y. Chao and S. Guo, *Energy Lab*, 2023, **1**, 220004.
22 D. Bellotti, L. Cassettari, M. Mosca and L. Magistri, *J. Cleaner Prod.*, 2019, **240**, 117947.
23 B. C. Yang, S. E. Jo, T. Kim, G. Park, D. Go, T. M. Gür and J. An, *J. Alloys Compd.*, 2022, **921**, 166078.
24 X. Du, M. Tan, T. Wei, H. Kobayashi, J. Song, Z. Peng, H. Zhu, Z. Jin, R. Li and W. Liu, *Chem. Eng. J.*, 2023, **452**, 139404.
25 J. Chang, L. Feng, C. Liu, W. Xing and X. Hu, *Energy Environ. Sci.*, 2014, **7**, 1628–1632.
26 J. Li, S. Wang, B. Zhang, W. Wang and L. Feng, *Int. J. Hydrogen Energy*, 2017, **42**, 12236–12245.
27 T. Xia, K. Zhao, Y. Zhu, X. Bai, H. Gao, Z. Wang, Y. Gong, M. Feng, S. Li, Q. Zheng, S. Wang, R. Wang and H. Guo, *Adv. Mater.*, 2023, **35**, 2206508.
28 S. Yu, S. Xu, R. Khan, H. Zhao and C. Li, *Catal. Sci. Technol.*, 2024, **14**, 820–834.
29 Y. Zhou, Q. Wang, X. Tian, J. Chang and L. Feng, *J. Energy Chem.*, 2022, **75**, 46–54.
30 W. Qiao, L. Yu, J. Chang, F. Yang and L. Feng, *Chin. J. Catal.*, 2023, **51**, 113–123.
31 Y. Kuang, W. Qiao, S. Wang, F. Yang and L. Feng, *ACS Mater. Lett.*, 2024, **6**, 1722–1731.
32 B. Zhu, B. Dong, F. Wang, Q. Yang, Y. He, C. Zhang, P. Jin and L. Feng, *Nat. Commun.*, 2023, **14**, 1686.
33 S. Wu, N. Salmon, M. M. Li, R. Bañares Alcántara and S. C. E. Tsang, *ACS Energy Lett.*, 2022, **7**, 1021–1033.
34 J. M. Spurgeon and B. Kumar, *Energy Environ. Sci.*, 2018, **11**, 1536–1551.

35 D. A. Bulushev and J. R. H. Ross, *ChemSusChem*, 2018, **11**, 821–836.
36 W. Wei, Z. Wei, R. Li, H. Yuan, J. Chen, J. Lv and S. Ouyang, *Green Carbon*, 2024, DOI: **10.1016/j.greenca.2024.05.003**.
37 R. Li, Y. Li, Z. Li, W. Wei, Q. Hao, Y. Shi, S. Ouyang, H. Yuan and T. Zhang, *ACS Catal.*, 2022, **12**, 5316–5326.
38 R. Li, Y. Li, Z. Li, W. Wei, S. Ouyang, H. Yuan and T. Zhang, *Sol. RRL*, 2021, **5**, 2000488.
39 Y. Li, R. Li, Z. Li, W. Wei, S. Ouyang, H. Yuan and T. Zhang, *Chem. Res. Chin. Univ.*, 2020, **36**, 1006–1012.
40 Y. X. Chen, A. Miki, S. Ye, H. Sakai and M. Osawa, *J. Am. Chem. Soc.*, 2003, **125**, 3680–3681.
41 W. Qiao, X. Huang and L. Feng, *Chin. J. Struct. Chem.*, 2022, **41**, 2207016–2207034.
42 X. Zhang, L. Hui, D. Yan, J. Li, X. Chen, H. Wu and Y. Li, *Angew. Chem., Int. Ed.*, 2023, **62**, e202308968.
43 X. Yang, J. Xue and L. Feng, *Chem. Commun.*, 2019, **55**, 11247–11250.
44 H. Chi, J. Lin, S. Kuang, M. Li, H. Liu, Q. Fan, T. Yan, S. Zhang and X. Ma, *J. Energy Chem.*, 2023, **85**, 267–275.
45 J. Shi, H. He, S. Zhou, J. Li and W. Cai, *Green Chem.*, 2024, **26**, 2638–2644.
46 J. Li, L. Li, J. Wang, A. Cabot and Y. Zhu, *ACS Energy Lett.*, 2024, **9**, 853–879.
47 T. Iwasita, *Electrochim. Acta*, 2002, **47**, 3663–3674.
48 D. Cao, G. Q. Lu, A. Wieckowski, S. A. Wasileski and M. Neurock, *J. Phys. Chem. B*, 2005, **109**, 11622–11633.
49 P. Ferrin and M. Mavrikakis, *J. Am. Chem. Soc.*, 2009, **131**, 14381–14389.
50 J. Wang, B. Zhang, W. Guo, L. Wang, J. Chen, H. Pan and W. Sun, *Adv. Mater.*, 2023, **35**, 2211099.
51 N. Ullah, S. Ullah, S. Khan, D. Guziejewski and V. Mirceski, *Int. J. Hydrogen Energy*, 2023, **48**, 3340–3354.
52 J. Wu, J. Wen and Y. X. Yu, *Appl. Surf. Sci.*, 2021, **565**, 150567.
53 J. M. Huo, Y. Wang, J. N. Xue, W. Y. Yuan, Q. G. Zhai, M. C. Hu, S. N. Li and Y. Chen, *Small*, 2024, **20**, 2305877.
54 X. Pang, H. Zhao, Y. Huang, B. Luo, H. Bai and W. Fan, *Appl. Surf. Sci.*, 2023, **608**, 155152.
55 H. Zhang, H. Wang, X. Tong, L. Zhou, X. Yang, Y. Wang, M. Zhang and Z. Wu, *Chem. Eng. J.*, 2023, **452**, 139582.
56 K. Deng, P. Liu, X. Liu, H. Li, W. Tian and J. Ji, *Green Chem.*, 2023, **25**, 9837–9846.
57 Q. Qian, X. He, Z. Li, Y. Chen, Y. Feng, M. Cheng, H. Zhang, W. Wang, C. Xiao, G. Zhang and Y. Xie, *Adv. Mater.*, 2023, **35**, 2300935.
58 W. Chen, Y. Wang, B. Wu, J. Shi, Y. Li, L. Xu, C. Xie, W. Zhou, Y.-C. Huang, T. Wang, S. Du, M. Song, D. Wang, C. Chen, J. Zheng, J. Liu, C.-L. Dong, Y. Zou, J. Chen and S. Wang, *Adv. Mater.*, 2022, **34**, 2105320.
59 B. Zhao, J. Liu, C. Xu, R. Feng, P. Sui, L. Wang, J. Zhang, J. Luo and X. Fu, *Adv. Funct. Mater.*, 2021, **31**, 2008812.
60 S. Ganguly, S. Paul, D. Khurana, T. S. Khan, P. K. Giri, C. Loha and S. Ghosh, *ACS Appl. Energy Mater.*, 2023, **6**, 5331–5341.
61 Y. Yi, J. Li and C. Cui, *Chin. Chem. Lett.*, 2022, **33**, 1006–1010.
62 G. Solomon, A. Landström, R. Mazzaro, M. Jugovac, P. Moras, E. Cattaruzza, V. Morandi, I. Concina and A. Vomiero, *Adv. Energy Mater.*, 2021, **11**, 2101324.
63 F. Meng, Q. Wu, K. Elouarzaki, S. Luo, Y. Sun, C. Dai, S. Xi, Y. Chen, X. Lin, M. Fang, X. Wang, D. Mandler and Z. J. Xu, *Sci. Adv.*, 2023, **9**, eadh9487.
64 Y. Zhou, Z. Wang, W. Fang, R. Qi, Z. Wang, C. Xia, K. Lei, B. You, X. Yang, Y. Liu, W. Guo, Y. Su, S. Ding and B. Y. Xia, *ACS Catal.*, 2023, **13**, 2039–2046.
65 B. Zhao, J. Liu, X. Wang, C. Xu, P. Sui, R. Feng, L. Wang, J. Zhang, J. Luo and X. Fu, *Nano Energy*, 2021, **80**, 105530.
66 L. Yang, J. Fan, B. Xiao and W. Zhu, *Chem. Eng. J.*, 2023, **468**, 143823.
67 H. Chen, Q. Wu, Y. Wang, Q. Zhao, X. Ai, Y. Shen and X. Zou, *Chem. Commun.*, 2022, **58**, 7730–7740.
68 V. Stamenkovic, B. S. Mun, K. J. J. Mayrhofer, P. N. Ross, N. M. Markovic, J. Rossmeisl, J. Greeley and J. K. Nørskov, *Angew. Chem., Int. Ed.*, 2006, **45**, 2897–2901.
69 B. Zhao, J. W. Liu, Y. R. Yin, D. Wu, J. L. Luo and X. Z. Fu, *J. Mater. Chem. A*, 2019, **7**, 25878–25886.
70 Y. Li, Z. Yin, M. Cui, X. Liu, J. Xiong, S. Chen and T. Ma, *J. Mater. Chem. A*, 2021, **9**, 2070–2092.
71 Y. Zhu, X. Wang, X. Zhu, Z. Wu, D. Zhao, F. Wang, D. Sun, Y. Tang, H. Li and G. Fu, *Small*, 2023, **19**, 2206531.
72 Y. Kuang, W. Qiao, F. Yang and L. Feng, *J. Energy Chem.*, 2023, **85**, 447–454.
73 H. Adamu, Z. H. Yamani and M. Qamar, *Mater. Renew. Sustain. Energy*, 2022, **11**, 169–213.
74 R. Yu, R. Shao, F. Ning, Y. Yu, J. Zhang, X.-Y. Ma, R. Zhu, M. Li, J. Lai, Y. Zhao, L. Zeng, J. Zhang and Z. Xia, *Small*, 2024, **20**, 2305817.
75 J. M. Martínez de la Hoz and P. B. Balbuena, *J. Phys. Chem. C*, 2011, **115**, 21324–21333.
76 H. Jin, C. Guo, X. Liu, J. Liu, A. Vasileff, Y. Jiao, Y. Zheng and S. Qiao, *Chem. Rev.*, 2018, **118**, 6337–6408.
77 B. Zheng, J. Fan, B. Chen, X. Qin, J. Wang, F. Wang, R. Deng and X. Liu, *Chem. Rev.*, 2022, **122**, 5519–5603.
78 A. A. Tedstone, D. J. Lewis and P. O'Brien, *Chem. Mater.*, 2016, **28**, 1965–1974.
79 N. B. Saleh, D. J. Milliron, N. Aich, L. E. Katz, H. M. Liljestrand and M. J. Kirisits, *Sci. Total Environ.*, 2016, **568**, 926–932.
80 C. Rao, H. Wang, K. Chen, H. Chen, S. Ci, Q. Xu and Z. Wen, *Small*, 2024, **20**, 2303300.
81 C. Xiao, L. Cheng, Y. Wang, J. Liu, R. Chen, H. Jiang, Y. Li and C. Li, *J. Mater. Chem. A*, 2022, **10**, 1329–1335.
82 C. Xie, D. Yan, H. Li, S. Du, W. Chen, Y. Wang, Y. Zou, R. Chen and S. Wang, *ACS Catal.*, 2020, **10**, 11082–11098.
83 H. Yun, M. Topsakal, A. Prakash, B. Jalan, J. S. Jeong, T. Birol and K. A. Mkhoyan, *Sci. Adv.*, 2021, **7**, eabd4449.
84 W. Li, D. Wang, Y. Zhang, L. Tao, T. Wang, Y. Zou, Y. Wang, R. Chen and S. Wang, *Adv. Mater.*, 2020, **32**, 1907879.
85 Y. Jia, K. Jiang, H. Wang and X. Yao, *Chem*, 2019, **5**, 1371–1397.

86 M. Khan, A. Hameed, A. Samad, T. Mushiana, M. I. Abdullah, A. Akhtar, R. S. Ashraf, N. Zhang, B. G. Pollet, U. Schwingenschlögl and M. Ma, *Commun. Chem.*, 2022, **5**, 109.
87 B. Liu, X. Wang, S. Wang, H. Peng, T. Xiao, G. Liu, S. Bai, Y. Zhao, W. Zhang and Y. Song, *Mater. Today Energy*, 2022, **28**, 101082.
88 T. R. Naveen Kumar, S. Kamalakannan, M. Prakash, B. Viswanathan and B. Neppolian, *ACS Appl. Energy Mater.*, 2022, **5**, 2104–2111.
89 J. Chen, M. Wang, B. Liu, Z. Fan, K. Cui and Y. Kuang, *J. Phys. Chem. B*, 2006, **110**, 11775–11779.
90 F. Liu and Z. Fan, *Chem. Soc. Rev.*, 2023, **52**, 1723–1772.
91 H. Qin, W. Tong, Q.-X. Pei, Z. Wang, G. Zhang, Y. Chen, P. Li, J. Liu, Z. Xu and Y. Liu, *Adv. Funct. Mater.*, 2023, **33**, 2300210.
92 W. Wei, Z. Wei, R. Li, Z. Li, R. Shi, S. Ouyang, Y. Qi, D. L. Philips and H. Yuan, *Nat. Commun.*, 2022, **13**, 3199.
93 W. Chen, C. Xie, Y. Wang, Y. Zou, C.-L. Dong, Y.-C. Huang, Z. Xiao, Z. Wei, S. Du, C. Chen, B. Zhou, J. Ma and S. Wang, *Chem*, 2020, **6**, 2974–2993.
94 Y. Qi, Y. Zhang, L. Yang, Y. Zhao, Y. Zhu, H. Jiang and C. Li, *Nat. Commun.*, 2022, **13**, 4602.
95 S. Ni, H. Qu, Z. Xu, X. Zhu, H. Xing, L. Wang, J. Yu, H. Liu, C. Chen and L. Yang, *Appl. Catal., B*, 2021, **299**, 120638.
96 C. Li, Y. Liu, Z. Zhuo, H. Ju, D. Li, Y. Guo, X. Wu, H. Li and T. Zhai, *Adv. Energy Mater.*, 2018, **8**, 1801775.
97 X. Yue, S. Liping, H. Lihua and Z. Hui, *ACS Appl. Nano Mater.*, 2023, **6**, 10312–10321.
98 Y. Hao, D. Yu, S. Zhu, C. Kuo, Y. Chang, L. Wang, H. Chen, M. Shao and S. Peng, *Energy Environ. Sci.*, 2023, **16**, 1100–1110.
99 B. Zhao, J. Liu, C. Xu, R. Feng, P. Sui, J. Luo, L. Wang, J. Zhang, J. Luo and X. Fu, *Appl. Catal., B*, 2021, **285**, 119800.
100 S. Li, R. Ma, J. Hu, Z. Li, L. Liu, X. Wang, Y. Lu, G. E. Sterbinsky, S. Liu, L. Zheng, J. Liu, D. Liu and J. Wang, *Nat. Commun.*, 2022, **13**, 2916.
101 J. Xue, X. Wu and L. Feng, *Chem. Commun.*, 2022, **58**, 2371–2374.
102 Y. A. Awoke, M. C. Tsai, D. B. Adam, A. A. Ayele, S. C. Yang, W. H. Huang, J. L. Chen, C. W. Pao, C. Y. Mou, W. N. Su and B. J. Hwang, *Electrochim. Acta*, 2022, **432**, 141161.
103 M. Li, D. Zhang, Y. Yi, B. Xue and B. Liu, *Electrochim. Acta*, 2022, **423**, 140566.
104 N. Kakati, J. Maiti, S. H. Lee, S. H. Jee, B. Viswanathan and Y. S. Yoon, *Chem. Rev.*, 2014, **114**, 12397–12429.
105 Y. Wang, X. Yang, K. Wang, Z. Liu, X. Sun, J. Chen, S. Liu, X. Sun, J. Xie and B. Tang, *Green Chem.*, 2023, **25**, 8216–8225.
106 Y. Zhou, K. Zhao, C. Shi, H. Ma, D. Yuan and Z. Yi, *J. Electrochem. Soc.*, 2024, **171**, 056506.
107 Y. Zhang, X. Wu, G. Fu, F. Si, X. Fu and J. Luo, *Int. J. Hydrogen Energy*, 2022, **47**, 17150–17160.
108 N. Cai, L. Fu, Z. Yang and D. Huang, *Curr. Opin. Electrochem.*, 2022, **34**, 100994.
109 Y. Zhang, J. Yang, R. Ge, J. Zhang, J. M. Cairney, Y. Li, M. Zhu, S. Li and W. Li, *Coord. Chem. Rev.*, 2022, **461**, 214493.
110 G. Fu, X. Kang, Y. Zhang, X. Yang, L. Wang, X. Fu, J. Zhang, J. Luo and J. Liu, *Nano-Micro Lett.*, 2022, **14**, 200.
111 D. Li, H. Liu and L. Feng, *Energy Fuels*, 2020, **34**, 13491–13522.
112 J. Li, S. Wang, J. Chang and L. Feng, *Adv. Powder Mater.*, 2022, **1**, 100030.
113 M. I. Abdullah, A. Hameed, N. Zhang, M. H. Islam, M. Ma and B. G. Pollet, *ACS Appl. Mater. Interfaces*, 2021, **13**, 30603–30613.
114 J. Luo, D. A. Vermaas, D. Bi, A. Hagfeldt, W. A. Smith and M. Grätzel, *Adv. Energy Mater.*, 2016, **6**, 1600100.
115 J. Zhu, L. Hu, P. Zhao, L. Y. S. Lee and K. Y. Wong, *Chem. Rev.*, 2020, **120**, 851–918.
116 Y. Luo, Z. Zhang, M. Chhowalla and B. Liu, *Adv. Mater.*, 2022, **34**, 2108133.
117 Y. Wang, G. Qian, Q. Xu, H. Zhang, F. Shen, L. Luo and S. Yin, *Appl. Catal., B*, 2021, **286**, 119881.
118 J. Hao, J. Liu, D. Wu, M. Chen, Y. Liang, Q. Wang, L. Wang, X. Fu and J. Luo, *Appl. Catal., B*, 2021, **281**, 119510.
119 F. Meng, C. Dai, Z. Liu, S. Luo, J. Ge, Y. Duan, G. Chen, C. Wei, R. R. Chen, J. Wang, D. Mandler and Z. J. Xu, *eScience*, 2022, **2**, 87–94.
120 K. Xiang, Z. Song, D. Wu, X. Deng, X. Wang, W. You, Z. Peng, L. Wang, J. Luo and X. Fu, *J. Mater. Chem. A*, 2021, **9**, 6316–6324.
121 Y. H. Fang and Z. P. Liu, *ACS Catal.*, 2014, **4**, 4364–4376.
122 G. T. Burstein, *Corros. Sci.*, 2005, **47**, 2858–2870.
123 F. Guo, K. Ye, M. Du, X. Huang, K. Cheng, G. Wang and D. Cao, *Electrochim. Acta*, 2016, **210**, 474–482.
124 N. Meddings, M. Heinrich, F. Overney, J. Lee, V. Ruiz, E. Napolitano, S. Seitz, G. Hinds, R. Raccichini, M. Gaberšček and J. Park, *J. Power Sources*, 2020, **480**, 228742.
125 N. T. Suen, S. F. Hung, Q. Quan, N. Zhang, Y. J. Xu and H. M. Chen, *Chem. Soc. Rev.*, 2017, **46**, 337–365.
126 M. Li, X. Deng, K. Xiang, Y. Liang, B. Zhao, J. Hao, J. Luo and X. Fu, *ChemSusChem*, 2020, **13**, 914–921.
127 D. Wu, J. Hao, W. Wang, Y. Yu, X. Fu and J. Luo, *ChemSusChem*, 2021, **14**, 5450–5459.
128 Y. Liang, Z. Song, Y. Zhang, B. Zhao, X. Wang, K. Xiang, Z. Ge, X. Fu and J. Luo, *ACS Appl. Nano Mater.*, 2021, **4**, 8723–8732.
129 S. Jiang, T. Xiao, C. Xu, S. Wang, H. Peng, W. Zhang, B. Liu and Y. Song, *Small*, 2023, **19**, 2208027.
130 R. Yuan, J. Wang, X. Luo, G. Wang, D. Wang, S. Liu and Z. Zhao, *Energy Fuels*, 2024, **38**, 1496–1507.
131 J. Li, *Electrochem. Commun.*, 2023, **146**, 107416.
132 C. Cao, D. Ma, J. Jia, Q. Xu, X. Wu and Q. Zhu, *Adv. Mater.*, 2021, **33**, 2008631.
133 C. Zhou, H. Yuan, P. Hu and H. Wang, *Chem. Commun.*, 2020, **56**, 15201–15204.
134 Y. Xu, M. Liu, M. Wang, T. Ren, K. Ren, Z. Wang, X. Li, L. Wang and H. Wang, *Appl. Catal., B*, 2022, **300**, 120753.
135 M. Zhou, C. Li and J. Fang, *Chem. Rev.*, 2021, **121**, 736–795.

136 L.-W. Chen and L. Wang, *Catal. Sci. Technol.*, 2023, **13**, 4590–4614.
137 F. Arshad, A. Tahir, T. u. Haq, H. Duran, I. Hussain and F. Sher, *Energy Fuels*, 2023, **37**, 14161–14170.
138 F. Arshad, A. Tahir, T. u. Haq, H. Duran, I. Hussain and F. Sher, *Int. J. Hydrogen Energy*, 2022, **47**, 36118–36128.
139 J. Chen, M. Ahmad, Y. Zhang, H. Ye, L. Wang, J. Zhang, X. Fu and J. Luo, *Chem. Eng. J.*, 2023, **454**, 140056.
140 S. A. Krishna, N. Noble, N. Radhika and B. Saleh, *J. Manuf. Process.*, 2024, **109**, 583–606.
141 S. Wang, L. Zhao, J. Li, X. Tian, X. Wu and L. Feng, *J. Energy Chem.*, 2022, **66**, 483–492.
142 J. Li, Y. Chang, D. Li, L. Feng and B. Zhang, *Chem. Commun.*, 2021, **57**, 7035–7038.
143 J. Li, S. Wang, S. Sun, X. Wu, B. Zhang and L. Feng, *J. Mater. Chem. A*, 2022, **10**, 9308–9326.
144 J. Zhang, Y. Hua, H. Li, X. Zhang, C. Shi, Y. Li, L. Di and Z. Wang, *Chem. Eng. J.*, 2023, **478**, 147288.
145 X. Wang, C. Xiao, Y. Li, T. Murayama, T. Ishida, M. Lin and G. Xiu, *Appl. Catal., A*, 2023, **664**, 119341.
146 S. Royer, D. Duprez, F. Can, X. Courtois, C. Batiot-Dupeyrat, S. Laassiri and H. Alamdari, *Chem. Rev.*, 2014, **114**, 10292–10368.
147 T. Q. N. Tran, S. W. Yoon, B. J. Park and H. H. Yoon, *J. Electroanal. Chem.*, 2018, **818**, 76–83.
148 L. Gong, N. Xuan, G. Gu, P. Lv, N. Huang, C. Song, M. Zheng, J. Wang, P. Cui, G. Gu, Y. Jia, G. Cheng and Z. Du, *Nano Energy*, 2023, **107**, 108124.
149 L. Ming, X. Wu, S. Wang, W. Wu and C. Lu, *ChemElectroChem*, 2022, **9**, e202200522.
150 Y. Fan, X. Yang, E. Wei, Y. Dong, H. Gao, X. Luo and W. Yang, *Appl. Catal., B*, 2024, **345**, 123716.
151 L. Yang, Z. Liu, S. Zhu, L. Feng and W. Xing, *Mater. Today Phys.*, 2021, **16**, 100292.
152 Y. Wang, M. Zhang, Y. Liu, Z. Zheng, B. Liu, M. Chen, G. Guan and K. Yan, *Adv. Sci.*, 2023, **10**, 2207519.
153 D. P. Sahoo, K. K. Das, S. Mansingh, S. Sultana and K. Parida, *Coord. Chem. Rev.*, 2022, **469**, 214666.
154 B. Liu, T. Xiao, X. Sun, H. Peng, X. Wang, Y. Zhao, W. Zhang and Y. Song, *J. Mater. Chem. A*, 2022, **10**, 19649–19661.
155 J. Masa and W. Schuhmann, *ChemCatChem*, 2019, **11**, 5842–5854.
156 T. Qin, Z. Wang, Y. Wang, F. Besenbacher, M. Otyepka and M. Dong, *Nano-Micro Lett.*, 2021, **13**, 183.
157 J. Li, R. Wei, X. Wang, Y. Zuo, X. Han, J. Arbiol, J. Llorca, Y. Yang, A. Cabot and C. Cui, *Angew. Chem.*, 2020, **59**, 20826–20830.
158 H. Wang, J. Li, K. Li, Y. Lin, J. Chen, L. Gao, V. Nicolosi, X. Xiao and J. Lee, *Chem. Soc. Rev.*, 2021, **50**, 1354–1390.
159 S. Dong, X. Chen, X. Zhang and G. Cui, *Coord. Chem. Rev.*, 2013, **257**, 1946–1956.
160 S. V. Didziulis, K. D. Butcher and S. S. Perry, *Inorg. Chem.*, 2003, **42**, 7766–7781.
161 L. Zhao, Q. Sun, M. Li, Y. Zhong, P. Shen, Y. Lin and K. Xu, *Sci. China Mater.*, 2023, **66**, 1820–1828.
162 J. Chang, L. Feng, C. Liu, W. Xing and X. Hu, *Angew. Chem., Int. Ed.*, 2014, **53**, 122–126.
163 J. Luo, K. Liang, Q. Zeng, L. Tang, Y. Yang, J. Song, S. Liu, S. Li, L. Hu and Y. Fang, *Appl. Surf. Sci.*, 2024, **654**, 159433.
164 X. Li, Z. Niu, M. Niu, J. Wang, D. Cao and X. Zeng, *Small*, 2024, **20**, 2311335.
165 Z. Duan, T. Ren, Q. Mao, H. Yu, K. Deng, Y. Xu, Z. Wang, L. Wang and H. Wang, *J. Mater. Chem. A*, 2022, **10**, 18126–18131.
166 J. Chang, W. Wang, D. Wu, F. Xu, K. Jiang, Y. Guo and Z. Gao, *J. Colloid Interface Sci.*, 2023, **648**, 259–269.
167 B. Zhao, C. Xu, M. Shakouri, R. Feng, Y. Zhang, J. Liu, L. Wang, J. Zhang, J. Luo and X. Fu, *Appl. Catal., B*, 2022, **305**, 121082.
168 J. Li, X. Tian, X. Wang, T. Zhang, M. C. Spadaro, J. Arbiol, L. Li, Y. Zuo and A. Cabot, *Inorg. Chem.*, 2022, **61**, 13433–13441.
169 F. Si, J. Liu, Y. Zhang, B. Zhao, Y. Liang, X. Wu, X. Kang, X. Yang, J. Zhang, X. Fu and J. Luo, *Small*, 2023, **19**, 2205257.
170 X. Peng, Y. Yan, X. Jin, C. Huang, W. Jin, B. Gao and P. K. Chu, *Nano Energy*, 2020, **78**, 105234.
171 C. Yang, Y. Lu, W. Duan, Z. Kong, Z. Huang, T. Yang, Y. Zou, R. Chen and S. Wang, *Energy Fuels*, 2021, **35**, 14283–14303.
172 X. Xia, L. Wang, N. Sui, V. L. Colvin and W. W. Yu, *Nanoscale*, 2020, **12**, 12249–12262.
173 R. A. Hussain and I. Hussain, *J. Solid State Chem.*, 2019, **277**, 316–328.
174 T. Lu, S. Dong, C. Zhang, L. Zhang and G. Cui, *Coord. Chem. Rev.*, 2017, **332**, 75–99.
175 J. Li, C. Xing, Y. Zhang, T. Zhang, M. C. Spadaro, Q. Wu, Y. Yi, S. He, J. Llorca, J. Arbiol, A. Cabot and C. Cui, *Small*, 2021, **17**, 2006623.
176 W. Liao, S. Wang, H. Su and Y. Zhang, *Nano Res.*, 2023, **16**, 1984–1991.
177 Y. Zhang, F. Gao, D. Wang, Z. Li, X. Wang, C. Wang, K. Zhang and Y. Du, *Coord. Chem. Rev.*, 2023, **475**, 214916.
178 A. Song, S. Song, M. Duanmu, H. Tian, H. Liu, X. Qin, G. Shao and G. Wang, *Small Sci.*, 2023, **3**, 2300036.
179 G. Zhang, B. Wang, L. Li, S. Yang, J. Liu and S. Yang, *J. Mater. Chem. A*, 2020, **8**, 18945–18954.
180 Y. Duan, X. L. Zhang, F. Y. Gao, Y. Kong, Y. Duan, X. T. Yang, X. X. Yu, Y. R. Wang, S. Qin, Z. Chen, R. Wu, P. P. Yang, X. S. Zheng, J. F. Zhu, M. R. Gao, T. B. Lu, Z. Y. Yu and S. H. Yu, *Angew. Chem.*, 2023, **62**, e202217275.
181 X. Ding, R. Jiang, J. Wu, M. Xing, Z. Qiao, X. Zeng, S. Wang and D. Cao, *Adv. Funct. Mater.*, 2023, **33**, 2306786.
182 Y. Qi, Y. Zhu, H. Jiang and C. Li, *Chin. J. Catal.*, 2024, **56**, 139–149.
183 S. Liu, S. Yin, L. Cui, H. Yu, K. Deng, Z. Wang, Y. Xu, L. Wang and H. Wang, *Energy Lab*, 2023, **1**, 220005.
184 C. Wan, J. Jin, X. Wei, S. Chen, Y. Zhang, T. Zhu and H. Qu, *J. Mater. Sci. Technol.*, 2022, **124**, 102–108.
185 M. Li, X. Deng, Y. Liang, K. Xiang, D. Wu, B. Zhao, H. Yang, J. Luo and X. Fu, *J. Energy Chem.*, 2020, **50**, 314–323.

186 Y. Zhang, X. Wu, G. Fu, X. Fu and J. Luo, *J. Alloys Compd.*, 2022, **906**, 164305.
187 M. Jiang, H. Zhai, L. Chen, L. Mei, P. Tan, K. Yang and J. Pan, *Adv. Funct. Mater.*, 2023, **33**, 2302621.
188 A. H. Al Naggar, N. M. Shinde, J. S. Kim and R. S. Mane, *Coord. Chem. Rev.*, 2023, **474**, 214864.
189 M. Ahmad, M. B. Hussain, J. Chen, Y. Yang, X. Wu, H. Chen, S. Afzal, W. Raza, Z. Zeng, F. Ye, X. Zhao, J. Zhang, R. Feng, X. Fu and J. Luo, *ACS Catal.*, 2024, **14**, 9134–9143.
190 Q. Yang, C. Zhang, B. Dong, Y. Cui, F. Wang, J. Cai, P. Jin and L. Feng, *Appl. Catal., B*, 2021, **296**, 120359.
191 M. Khan, M. I. Abdullah, A. Samad, Z. Shao, T. Mushiana, A. Akhtar, A. Hameed, N. Zhang, U. Schwingenschlögl and M. Ma, *Small*, 2023, **19**, 2205499.
192 J. Tian, C. Cao, D. Ma, S. Han, Y. He, X. Wu and Q. Zhu, *Small Struct.*, 2022, **3**, 2100134.
193 M. Zhang, J. Zhu, R. Wan, B. Liu, D. Zhang, C. Zhang, J. Wang and J. Niu, *Chem. Mater.*, 2022, **34**, 959–969.
194 X. Wang, S. Xi, P. Huang, Y. Du, H. Zhong, Q. Wang, A. Borgna, Y. W. Zhang, Z. Wang, H. Wang, Z. G. Yu, W. S. V. Lee and J. Xue, *Nature*, 2022, **611**, 702–708.
195 C. Lin, J. Li, X. Li, S. Yang, W. Luo, Y. Zhang, S. H. Kim, D. H. Kim, S. S. Shinde, Y. F. Li, Z. P. Liu, Z. Jiang and J. H. Lee, *Nat. Catal.*, 2021, **4**, 1012–1023.
196 L. Zhang, L. Wang, H. Lin, Y. Liu, J. Ye, Y. Wen, A. Chen, L. Wang, F. Ni, Z. Zhou, S. Sun, Y. Li, B. Zhang and H. Peng, *Angew. Chem., Int. Ed.*, 2019, **58**, 16820–16825.
197 S. K. Geng, Y. Zheng, S. Q. Li, H. Su, X. Zhao, J. Hu, H. B. Shu, M. Jaroniec, P. Chen, Q. H. Liu and S. Z. Qiao, *Nat. Energy*, 2021, **6**, 904–912.

